Lawrence Berkeley National Laboratory
LBL Publications

Title
Characterizing Shallow Attenuation and Microearthquake Source Parameters Using a Downhole DAS Array at the Cape Modern Geothermal Field

Permalink
https://escholarship.org/uc/item/5mz2s5wx

Journal
Journal of Geophysical Research: Solid Earth, 131(9)

ISSN
2169-9313

Authors
Chang, Hilary
Nakata, Nori
Abercrombie, Rachel E
et al.

Publication Date
2026-09-01

DOI
10.1029/2026jb034276

Copyright Information
This work is made available under the terms of a Creative Commons Attribution License, available at https://creativecommons.org/licenses/by/4.0/

Peer reviewed

eScholarship.org Powered by the California Digital Library
University of California

Check for updates

JGR Solid Earth

RESEARCH ARTICLE
10.1029/2026JB034276

Characterizing Shallow Attenuation and Microearthquake Source Parameters Using a Downhole DAS Array at the Cape Modern Geothermal Field

Hilary Chang[1], Nori Nakata[2], Rachel E. Abercrombie[3], Sireesh Dadi[4], and Aleksei Titov[4]

[1]Lamont-Doherty Earth Observatory, Palisades, NY, USA, [2]Lawrence Berkeley National Laboratory, Berkeley, CA, USA, [3]Boston University, Boston, MA, USA, [4]Fervo Energy, Houston, TX, USA

Key Points:

- We obtain the first high-resolution attenuation structure in the top 2.5 km from seismic observation
- Borehole fiber-optic cable captures a broad bandwidth, which is advantageous for modeling microearthquakes
- The channel-dependent gauge length and directivity effects can introduce uncertainty in source characterization

Supporting Information:

Supporting Information may be found in the online version of this article.

Correspondence to:

H. Chang,
hilarych@ldeo.columbia.edu

Citation:

Chang, H., Nakata, N., Abercrombie, R. E., Dadi, S., & Titov, A. (2026). Characterizing shallow attenuation and microearthquake source parameters using a downhole DAS array at the Cape Modern geothermal field. *Journal of Geophysical Research: Solid Earth*, *131*, e2026JB034276. https://doi.org/10.1029/2026JB034276

Received 18 MAR 2026
Accepted 24 AUG 2026

Author Contributions:

Conceptualization: Hilary Chang, Nori Nakata, Rachel E. Abercrombie
Data curation: Hilary Chang, Sireesh Dadi, Aleksei Titov
Formal analysis: Hilary Chang
Funding acquisition: Hilary Chang, Nori Nakata
Investigation: Hilary Chang
Methodology: Hilary Chang, Rachel E. Abercrombie
Project administration: Nori Nakata, Sireesh Dadi, Aleksei Titov
Resources: Nori Nakata
Supervision: Nori Nakata, Rachel E. Abercrombie

© 2026 The Author(s). Journal of Geophysical Research: Solid Earth published by Wiley Periodicals LLC on behalf of American Geophysical Union. This is an open access article under the terms of the Creative Commons Attribution License, which permits use, distribution and reproduction in any medium, provided the original work is properly cited.

Abstract Earthquake source parameters are crucial for assessing seismic hazard and understanding earthquake source physics. However, source parameter estimation is challenging for small earthquakes because they suffer notorious trade-offs with shallow attenuation. Borehole Distributed Acoustic Sensing (DAS) uses fiber-optic cables to provide unprecedented spatial resolution for attenuation analysis and a closer recording of the earthquake source. In this study, we use DAS in a vertical well in the Cape Modern geothermal field, near Milford, Utah, to characterize shallow attenuation and estimate source parameters of microearthquakes ($0 < M < 1.7$) that occurred during a stimulation. We directly correct the DAS instrument response and directional sensitivity. We use along-depth spectral ratios to obtain a high-resolution Quality Factor (Q) profile for P waves in the top 2,500 m. We find low Q at the near surface, and that attenuation primarily decreases with depth, with less dependence on rock types, consistent with previous studies in California and Switzerland. We use a single-spectral approach to estimate corner frequency, source radius, slip, magnitude, and spectral stress drop over the limited magnitude range. The spectral stress drops do not show magnitude dependence, while their variability might relate to fault heterogeneity or rupture variability. The DAS response-correction is channel-dependent and can introduce biases in source parameters. We reduce potential biases by using channels with similar responses and checking measurement consistency. We use the Empirical Green's Function for two event pairs to benchmark the results. This work shows the potential of using DAS for understanding crustal attenuation and characterizing microearthquakes.

Plain Language Summary Seismic hazard assessment requires a good understanding of earthquake source physics and how seismic energy scales with magnitudes. This information is encapsulated in source parameters such as the spectral stress drop, which is a measure of the static stress released during earthquakes. However, characterizing small earthquakes is challenging because of potential biases from wave propagation effects. The attenuation, which is often poorly known, is the main source of inconsistency in spectral stress drops for small earthquakes. In this study, we demonstrate the potential of using a fiber-optic cable deployed in the borehole with Distributed Acoustic Sensing (DAS) to analyze shallow attenuation and microearthquakes in a geothermal reservoir. The downhole DAS provides an unprecedentedly dense seismic network in the subsurface and a closer recording of the small earthquakes. We obtain the first high-resolution attenuation structure from seismic observation. The near-surface high attenuation echoes the importance of accounting for shallow attenuation when modeling the seismograms. The spectral stress drop variation likely characterizes the subsurface heterogeneity or comes from more complex sources. We show that downhole DAS can provide new attenuation observations in the crust and improve our ability to model small earthquakes if we carefully account for the instrument response of the cable.

1. Introduction

To understand source physics and assess seismic hazard, we need to quantify and characterize the source of observed earthquakes. These characteristics are earthquake source parameters. The source dimension and the earthquake size are characterized by the corner frequency and magnitude, respectively. The shear stress released on the fault during the rupture is the stress drop. For induced earthquakes, these parameters reveal the subsurface response to human activities. In the Enhanced Geothermal System (EGS), stimulation induces small events that illuminate the fractures. Microearthquakes ($M < 2$) carry information on the stress condition of the fault, the energy released, and can reveal potential structural anomalies.

Validation: Hilary Chang
Visualization: Hilary Chang
Writing – original draft: Hilary Chang
Writing – review & editing: Hilary Chang, Nori Nakata, Rachel E. Abercrombie

However, source characterization for small earthquakes has proved challenging (see, e.g., review by Abercrombie, 2021; Abercrombie et al., 2025). The difficulty comes from many effects that are difficult to separate from each other in seismic observation. The observed earthquake Fourier spectrum $U(f)$ (f is frequency) can be expressed in general by

$$U(f) = S(f) \cdot P(f) \cdot G(f) \cdot I(f), \quad (1)$$

where $S(f)$ is the source effect, $P(f)$ and $G(f)$ are the path and site effects that relate to wave propagation, and $I(f)$ is the instrument response. The path effect is travel-time dependent and varies with distances between the earthquake and the station. The site effect occurs at shallow depths beneath a station and is common for all events recorded at the station. For microearthquakes, attenuation is the major wave propagation effect that can result in significant bias in source modeling. This is because attenuation dominates at the high-frequency amplitudes (>10 Hz) where the corner frequency lies. Biases in corner frequency due to uncertainty of near-surface structure have been found to be the most significant reason for inconsistency between spectral stress drop estimates in different studies of small earthquakes (Abercrombie & Baltay, 2025; Abercrombie et al., 2025; Shearer et al., 2025). Failing to account for the large shallow attenuation can result in trade-offs that lead to systematic biases in corner frequency and spectral stress drop (Abercrombie, 1997; Abercrombie & Leary, 1993; Ahn et al., 2025; Chang et al., 2023, 2025; Ko et al., 2012; Shearer et al., 2019).

The problem is, most of the time, we have very limited knowledge of seismic attenuation in the subsurface. Previous studies measured attenuation using downhole geophones and seismometers and found attenuation to be more dependent on depth than on rock type (Abercrombie, 1997). A very low Q at the surface, increasing rapidly with depth (i.e., attenuation decreases), is observed at Parkfield (Jongmans & Malin, 1995), Cajon Pass in Southern California (Abercrombie, 1997), and Basel in Switzerland (Bethmann et al., 2012). Still, the along-depth attenuation is poorly constrained because the sensors are sparsely spaced (hundreds of meters apart). Because of the lack of attenuation structure information, studies often have to make assumptions in earthquake source characterization. Chang et al. (2025) demonstrated that failing to separate path- and site-dependent attenuation can lead to systematic bias in corner-frequency estimates. Shearer et al. (2025) showed that different attenuation corrections can result in widely different source spectra. To date, the spectral stress drop is still a largely unconstrained parameter (Abercrombie & Baltay, 2025; Abercrombie et al., 2025).

Recently, advances in Distributed Acoustic Sensing (DAS) for earthquake seismology offer a great tool for downhole monitoring (Zhan, 2020). The DAS captures the seismic waves as strain rate (or strain) along the fiber-optic cable (Hartog, 2017). The cable can be installed behind the well casing and provide densely distributed downhole sensors (a few meters spacing). The optic fiber needs lower maintenance compared to the electric sensors (M. Li et al., 2015). Hence, we can use these fiber-optic cables to achieve dense seismic networks in the subsurface. This gives us a great opportunity to resolve the along-depth attenuation with high spatial resolution. In addition, the downhole cable allows us to observe microearthquakes in situ, minimizing the contamination from wave propagation effects.

In this study, we use DAS in a vertical borehole to measure attenuation as a function of depth and characterize source parameters for microearthquakes that occurred during stimulation in a geothermal field. These analyses involve modeling the DAS amplitude spectra, which have been relatively less explored. Unlike geophones and seismometers that measure particle motions, DAS measure "strain," which is more sensitive to motion along the cable direction (the directivity effect). The finite gauge length for measuring strain also causes a frequency-dependent sensitivity. Both effects alter amplitudes, while the phase is not affected (Bakku, 2015; Dean et al., 2017; Lindsey et al., 2020).

To avoid this complication in amplitude, DAS seismic applications have been focusing on phase analysis, including detecting and locating earthquakes (e.g., Karrenbach et al., 2019; Lellouch et al., 2019; Zhang et al., 2023; Zhu et al., 2023), structure imaging (e.g., Chang & Nakata, 2024; Correa et al., 2019; Martuganova et al., 2024; Park, Jung, et al., 2025; Park, Nakata, et al., 2025), and time-lapse changes (e.g., Byerley et al., 2018; Chang & Nakata, 2022; Daley et al., 2016; Mateeva et al., 2014). Studies that involved DAS amplitude focus on low-frequency (<10 Hz), where only the directivity effect is important while the gauge length effect is relatively small. These studies include earthquake magnitude estimation (Barbour et al., 2025; Gök et al., 2024; Lellouch et al., 2021; Lior, 2024; Lior et al., 2023; Nayak et al., 2024) and fracture characterization (Jin & Roy, 2017;

21699356, 2026, 9, Downloaded from https://agupubs.onlinelibrary.wiley.com/doi/10.1029/2026JB034276, Wiley Online Library on [23/10/2026]. See the Terms and Conditions (https://onlinelibrary.wiley.com/terms-and-conditions) on Wiley Online Library for rules of use; OA articles are governed by the applicable Creative Commons License

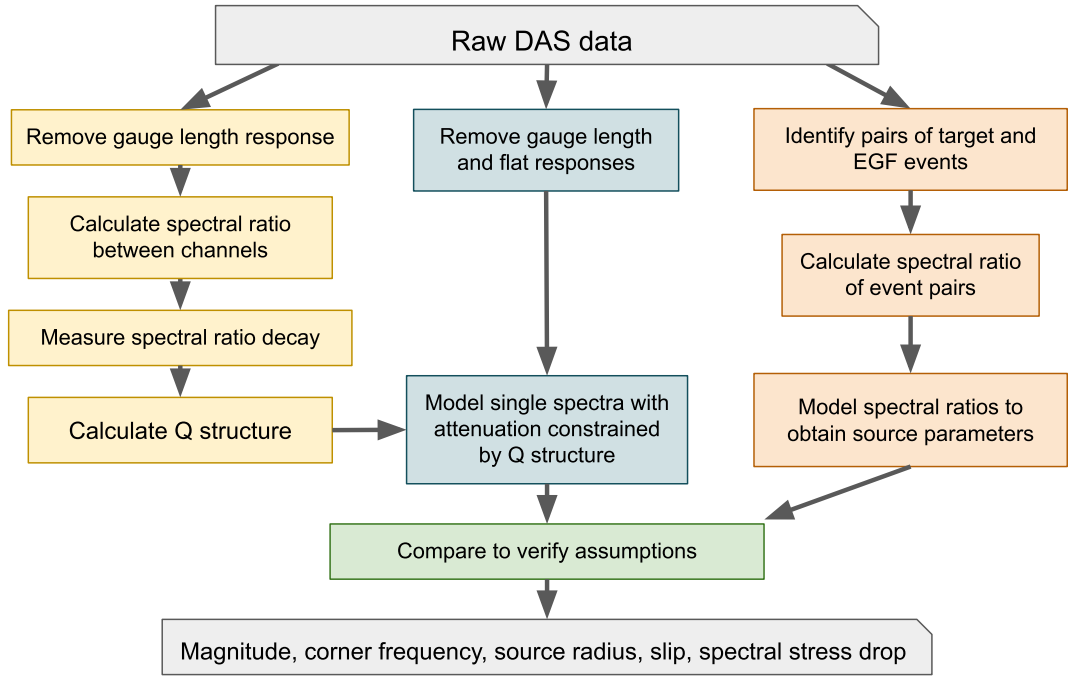


Figure 1. The workflow for analyzing shallow attenuation and modeling microearthquake source parameters in this study. Gray boxes with a clipped corner are data and final results. Rectangles are processes—Yellow: Attenuation analysis. Blue: Single spectral source parameter analysis. Orange: Empirical Green's Function (EGF) or spectral ratio source parameter analysis. Green: Verification between single-spectral and EGF methods.

Rodríguez Tribaldos et al., 2024; Zhan, 2020), and using polarities for focal mechanism determination (Cole et al., 2018; Baird et al., 2020; Luo et al., 2021; J. Li et al., 2023). Some studies used DAS data for source characterization with a spectral ratio approach (Barbour et al., 2025; Chen, 2023; Lior, 2024). They used the Empirical Green's Function (EGF) approach to remove the wave propagation effect and instrument response, which has been shown to be effective. However, finding a suitable EGF for small events can be difficult, and the EGF adds additional uncertainties (Abercrombie, 2015). Strumia et al. (2024) used a shallow buried horizontal cable in a dry lake to characterize earthquakes of M 2.0–4.3 without EGFs. They estimated relative lateral variability in shallow attenuation and then used it to constrain the source model. They also considered the cable directivity but not the gauge length effect because their interested frequency range is lower than 10 Hz. They showed the importance of considering local attenuation when estimating source parameters.

Similar to Strumia et al. (2024), here, we estimate attenuation and directly model the amplitude spectra to constrain source parameters, including corner frequency and magnitudes. The difference is that we can directly analyze variation in shallow Q with depth using a vertical cable. Also, we need to consider the gauge length effect as our earthquakes are small ($M < 2$) and their corner frequencies are expected to be at high frequencies (tens to hundreds of Hz) (Baltay et al., 2024; Kwiatek et al., 2014). We estimate source parameters by fitting the Brune model (Boatwright, 1978, 1980; Brune, 1970). This direct modeling approach is the single spectral method (e.g., Abercrombie, 1995; Ko et al., 2012; Yu et al., 2020). We use the two available event pairs to perform the EGF spectral ratio analysis to help benchmark the corner frequency estimates. Eventually, we map the source parameters of microearthquakes on the faults and discuss the potential implications of their variations.

This paper is structured into four sections. First, we introduce the microearthquakes at the Cape Modern geothermal field. Second, we discuss the role of the DAS responses in the attenuation and source parameter analysis. Third, we resolve the along-depth Q profile. Fourth, we perform the source parameter analysis by fitting the Brune model and verify the results using the spectral ratio approach. Figure 1 summarizes the workflow of the analysis.

21699356, 2026, 9, Downloaded from https://agupubs.onlinelibrary.wiley.com/doi/10.1029/2026JB034276, Wiley Online Library on [23/10/2026]. See the Terms and Conditions (https://onlinelibrary.wiley.com/terms-and-conditions) on Wiley Online Library for rules of use; OA articles are governed by the applicable Creative Commons License

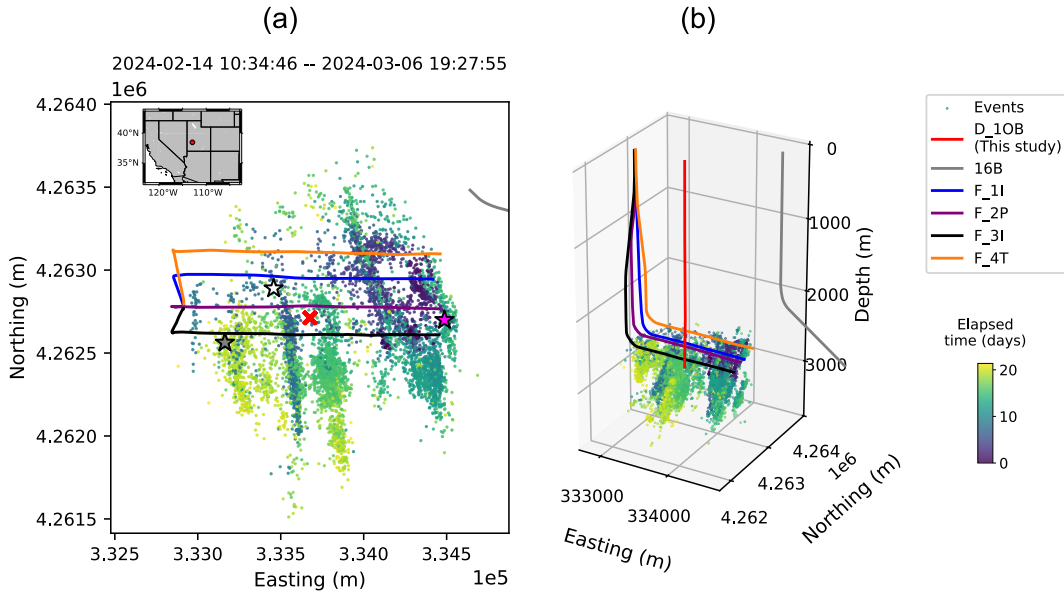


Figure 2. Configuration of the wells and the microearthquakes in (a) 2D and (b) 3D. Inset in (a) shows the site location in Utah (red dot). There are four L-shaped Frisco injection wells (F-1I, F-2P, F-3I, F-4T; color curves) and a vertical Delano well (D-1OB; red cross) that has a fiber-optic cable installed. The deviated production well (16B) is at the nearby FORGE geothermal site. The color dots are the ∼7,100 events that occurred during 27 stages of stimulation in wells F-1I and F-3I. The vertical and horizontal axes are 1:1. The example events are marked by the white (Event 1), the gray (Pair 1: Events 2,3), and the magenta (Pair 2: Events 4,5) stars (Table S1 in Supporting Information S1).

2. Microearthquakes at the Cape Modern Geothermal Field

The Cape Modern geothermal field is near Milford, Utah. Figure 2 shows the 2.5 km × 2.5 km area that includes four L-shaped Frisco injection wells and a vertical Deleno well (D-1OB). The vertical well has a fiber-optic cable installed. In the area of the map, thick basin sediments and volcanics cover a granite basement at 1,000–2,000 m depth (Fercho et al., 2024). The granite reaches 200–225°C at 2,500–3,000 m depth, which is the target of the EGS.

In February 2024, Fervo Energy performed the first stimulation in the L-shaped Frisco wells F-1I and F-3I (Dadi et al., 2024). Each well was stimulated with 27 stages, spanning from mid-February to mid-March. They detected and located ∼7,100 microearthquake events within 1.5 km horizontal distance from the injection wells during stimulation with magnitudes ranging from −0.6 to 2.9 (Nayak et al., 2026). The location was estimated using both surface geophones, regional networks (Nakata et al., 2024), and borehole DAS by Fervo Energy. The dominant focal mechanism is strike-slip with some normal faulting (Mohammadi et al., 2025), which is expected for the Basin and Range extensional regime. The seismicity is likely due to reactivation of pre-existing fractures (Dadi et al., 2024; Nakata et al., 2025). In this study, we are able to characterize ∼1,800 events (M_w 0–1.7) with hypocentral distance 0.7–2.2 km from the DAS channels used for source parameter estimation (1,800–2,400 m depth; Section 5).

We focus on analyzing the downhole DAS (Silixa iDAS) in the vertical well D-1OB. The cable is cemented behind the casing. The DAS system has 1,600 channels (i.e., stations) with a channel separation of approximately 2 m. The gauge length (L) is 10 m. The sampling rate (fst) is 1,000 Hz. The raw DAS data is *radian* per gauge length per second, and can be converted to strain rate (nm/m/s) by multiplying $2^{-13} \cdot fst/L$ for Silixa iDAS. We use a modified 1D velocity profile based on a previous seismic survey (Miller, 2018) to window the arrivals for picking and calculate travel time. Figure 3 shows the wavefield of a M_w 1.5 event (Event 1) recorded by the vertical DAS cable and the picked P-wave arrivals. See Text S1 in Supporting Information S1 for details on picking and windowing.

21699356, 2026, 9, Downloaded from https://agupubs.onlinelibrary.wiley.com/doi/10.1029/2026JB034276, Wiley Online Library on [23/10/2026]. See the Terms and Conditions (https://onlinelibrary.wiley.com/terms-and-conditions) on Wiley Online Library for rules of use; OA articles are governed by the applicable Creative Commons License

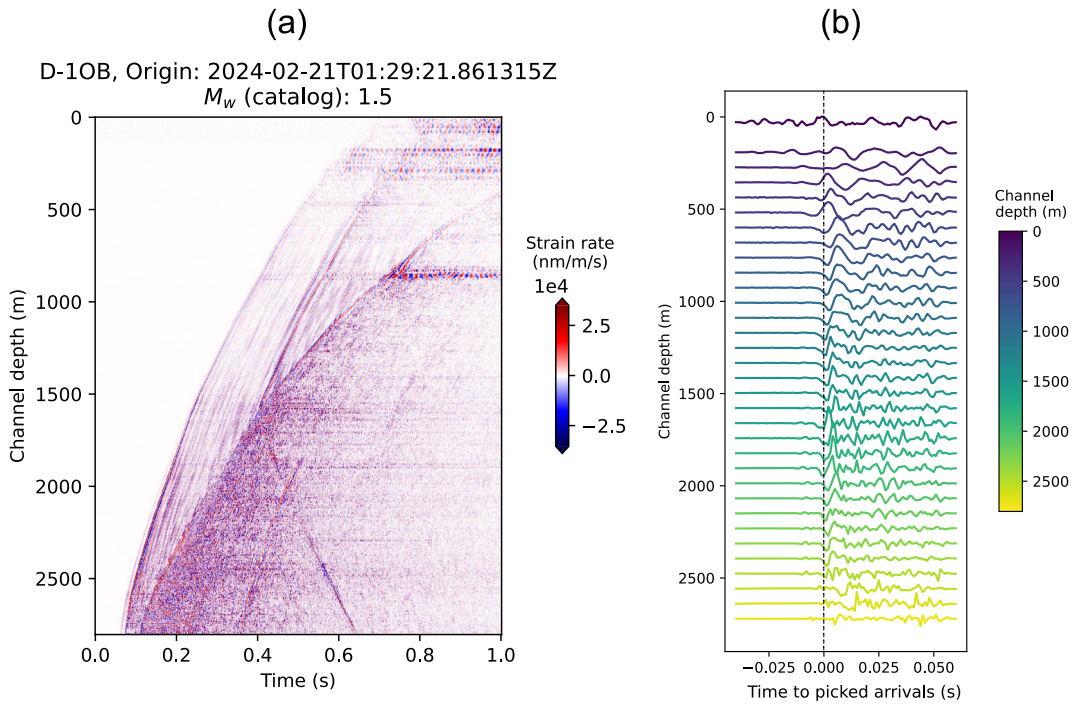


Figure 3. A microearthquake event (catalog $M_w = 1.5$, Event 1): (a) Wavefield captured by Distributed Acoustic Sensing in the vertical well D-1OB. Channel spacing is 2 m. (b) Raw P-wave arrivals (normalized by the maximum amplitude), aligned by the picked time (dashed line) of a kurtosis picker. We only show every 40 available picks for visualization.

3. Consideration of DAS Directivity, Gauge Length Effect, and Unit Conversion

We calculate the amplitude strain rate spectra using a multitaper method (Prieto, 2022). We use a P-wave time window of 0.1 s, sufficiently long to capture the low-frequency spectrum. The preprocessing includes demeaning (in space and time), detrending (in time), and tapering both ends of the trace (in time). The noise window starts 0.3 s before the P arrival with a duration of 0.1 s (Figure S1 in Supporting Information S1).

Figure 4a shows the DAS strain rate amplitude spectra. To convert the DAS strain rate to ground motion, we consider the following effects: (a) the source effect, (b) the flat response (Figure 4b), including directivity effect and a conversion from particle motion to its spatial gradient, (c) the gauge length effect (Figure 4c), and (d) the attenuation (Figure 4d). We assume the channels are in the farfield of the event and thus plane waves. The source is the far-field earthquake source spectra. Bakku (2015) showed both (b) and (c) and their combined version. Here, we group these effects by their spectral shape and highlight the controlling factors so that it is easier to understand how they cause potential biases for source parameter measurements later in the discussion (Section 6). In this paper, we use the broad term "response" to include both (b) and (c).

The flat response (Figure 4b) represents how the particle motion (acceleration) amplitude of the wave is observed as spatial gradient (strain rate) in the cable direction (described in Equation 3.4 in Bakku, 2015):

$$R_1 = 1/(S(\theta) \cdot v_{\text{app}}), \tag{2}$$

where θ is the incident angle (between the cable and the ray path). $S(\theta)$ is the particle motion sensitivity for P waves ($S(\theta) = 1/\cos(\theta)$) and S waves ($S(\theta) = 1/\sin(\theta)$). v_{app} is the apparent wave speed, used to convert particle motion to its spatial gradient (see Equation 6 in H. F. Wang et al., 2018). v_{app} can be estimated by dividing the channel separation by the arrival time difference between channels, or $v_{\text{app}} = v/\cos(\theta)$, where v is the wave speed (unit: m/s). We use the former method to calculate the actual v_{app}. The later method might be subject to the uncertainties of the velocity profile and the incident angle, although we test that both methods produce similar results. The flat response is channel-dependent and frequency-independent.

21699356, 2026, 9, Downloaded from https://agupubs.onlinelibrary.wiley.com/doi/10.1029/2026JB034276, Wiley Online Library on [23/10/2026]. See the Terms and Conditions (https://onlinelibrary.wiley.com/terms-and-conditions) on Wiley Online Library for rules of use; OA articles are governed by the applicable Creative Commons License

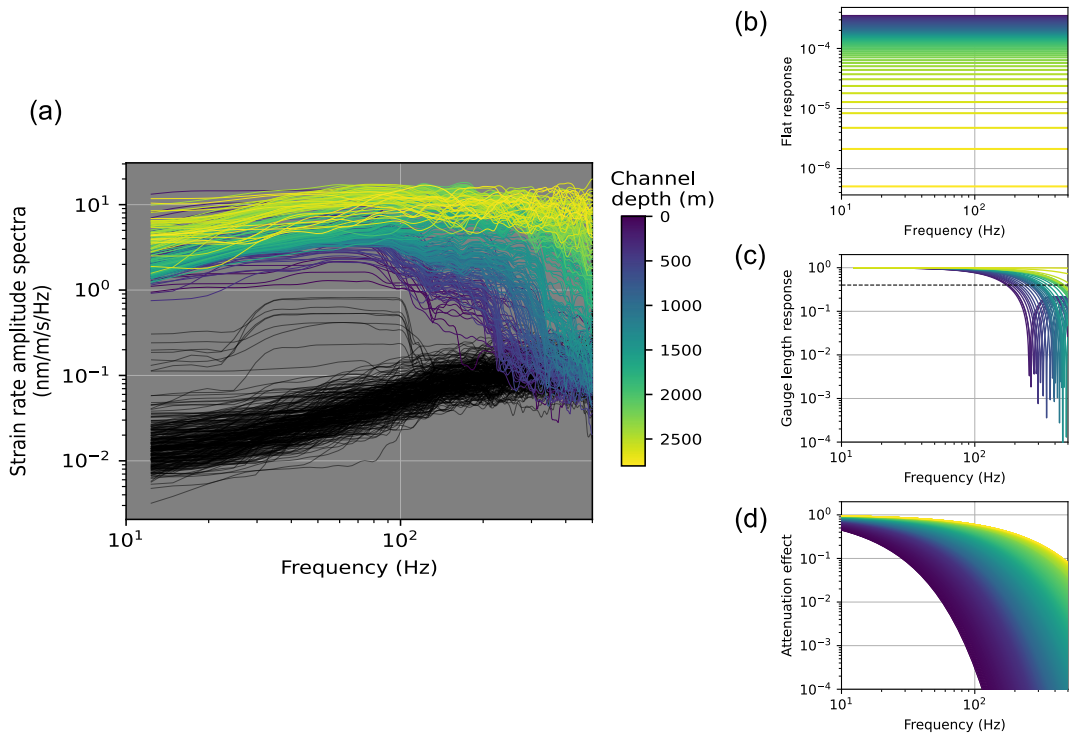


Figure 4. Earthquake P-wave spectra of the Distributed Acoustic Sensing strain rate data for Event 1 (catalog M_w 1.5) and the observational effects (in addition to the source effect). (a) P-wave amplitude strain rate spectra (color) and noise (black). We group the effects by their spectral shape: (b) The flat response that includes the cable directivity and a conversion from particle motion to its spatial gradient (Equation 2). (c) The gauge length effect (Equation 5). The horizontal dashed line is the cutoff amplitude (0.4) for water-level stabilization to avoid amplifying high-frequency noise when removing the gauge length effect. (d) Cumulative attenuation effect ($e^{-\pi f \kappa}$ with κ in Equation 7) depends on Q and travel time. The colorbar applies to all subfigures.

We can converts the strain rate ($\dot{\epsilon}$, unit: nm/m/s) to particle acceleration ($\ddot{u}$, unit: m/s^2) by:

$$\ddot{u} = \dot{\epsilon}/R_1 \cdot 10^{-9}. \tag{3}$$

To convert acceleration to displacement (u, unit: m), we follow Lior and Ziv (2018):

$$u = \ddot{u}/(2\pi f)^2, \tag{4}$$

where f is frequency.

The gauge length response (Figure 4c) is related to the frequency sensitivity due to the finite length for measuring strain (described in Equation 3.5 in Bakku, 2015)

$$R_2 = \mathrm{sinc}(\pi f L/v_{\mathrm{app}}), \tag{5}$$

where $\mathrm{sinc}(x) = \frac{\sin(x)}{x}$ (be careful that some software packages might use a different definition). L is the gauge length. R_2 also depends on gauge length and the apparent velocity, and is both channel and frequency dependent. We can remove the gauge length effect by dividing the data by R_2.

In the attenuation analysis (Section 4), we only consider R_2 because we only measure the relative spectral decay to get Q. In the single spectral source parameter analysis (Section 5.1), we consider both R_1 and R_2 because we need the spectra in the unit of m to fit the farfield source spectra model. In the EGF analysis (Section 5.2), we do not consider both responses as the EGF accounts for the responses.

21699356, 2026, 9, Downloaded from https://agupubs.onlinelibrary.wiley.com/doi/10.1029/2026JB034276, Wiley Online Library on [23/10/2026]. See the Terms and Conditions (https://onlinelibrary.wiley.com/terms-and-conditions) on Wiley Online Library for rules of use; OA articles are governed by the applicable Creative Commons License

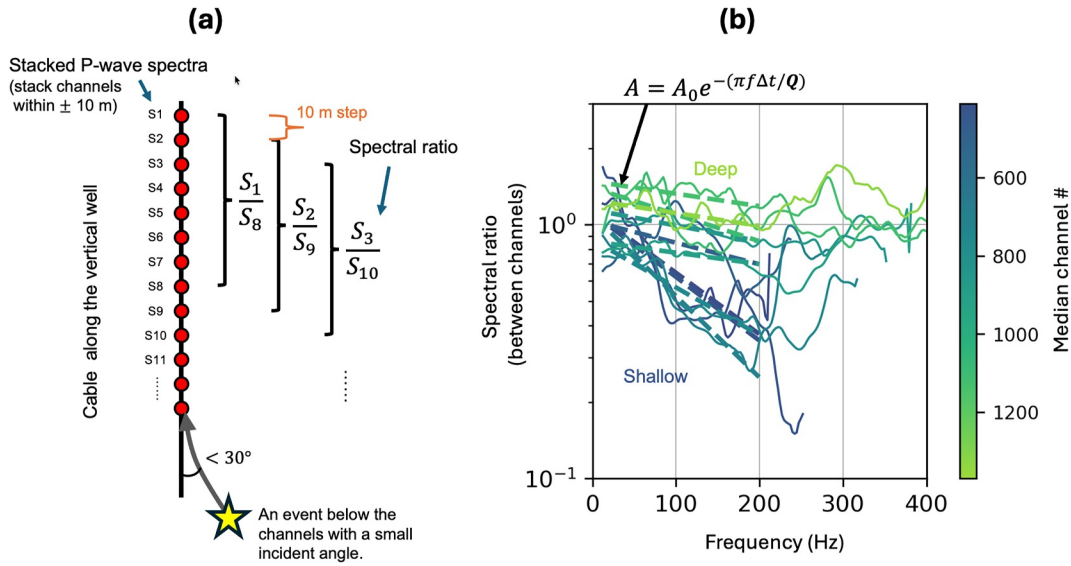


Figure 5. Illustration of the attenuation analysis. (a) We use P-wave arrivals with an incident angle <30°. After removing the gauge length effect, we stack P spectra every 20 m (red balls) and calculate the spectral ratio between channels separated by 160 m. (b) We fit the spectral ratio with an exponential function (Equation 6) between 20 and 200 Hz to estimate the Q values. Depth intervals between shallower channels (smaller channel #) show a larger decay (lower Q) in general.

4. Calculation of the Shallow Attenuation Structure

We use the amplitude decay between P-wave spectra recorded at different depths to estimate Q along the vertical well. As this method relies on the difference in frequency content at pairs of depths for individual events, it does not rely on the assumption of any particular source model or high-frequency fall-off. We take a 0.1 s P arrival window, demean (in space and time), detrend (in time), taper the trace (in time), and calculate the Fourier spectra. Then, we perform a spectral point-wise quality control to retain the bandwidth with signal-to-noise ratio (SNR) >3 (Viegas et al., 2010). We calculate v_{app} by dividing the channel separation by the arrival time difference between channels. Then, we remove the gauge length response by dividing the spectra by R_2 (Equation 5). To avoid amplifying noise, we set a high-frequency cutoff amplitude at a water level of 0.4 for the gauge response removal (horizontal dashed line in Figure 4c), and we discard channels where the cutoff frequency (where the response drops below the water level) < 200 Hz. We only use arrivals with incident angles less than 30° as we aim to characterize attenuation between channels. The travel time is calculated by ray-tracing (White et al., 2020) using a modified 1D velocity model based on Miller (2018). To enhance SNR, we stack P-wave spectra by taking the median P-wave spectra of every 20 m of channels. We take the median channel number, location, and arrival times to represent each 20 m stack.

We calculate channel-wise spectral ratios between stacked P-wave spectra that are 80 channels (~160 m) apart to find the attenuation in the interval in between (Figure 5). To be more specific, every P-wave spectrum of a 20 m stack is divided by another 20 m stack that is 80 channels below. The 80-channel separation applies to the median channel number of the stacks. We select this spacing and geometry to ensure resolvable attenuation in the depth intervals, and stacking of similar signals to amplify the signal. This spectral division process is repeated with a step of 10 m to have some overlap between measurements (the overlapping brackets in Figure 5a). We estimate frequency-independent Q by fitting the ratios with the following equation (Anderson & Hough, 1984),

$$A = A_0 e^{-\pi f \Delta t/Q}, \tag{6}$$

where A_0 is an arbitrary low-frequency amplitude, and Δt is the travel time difference between the two spectral stacks. We only fit the ratios between 20 and 200 Hz (the minimum cutoff frequency in the gauge length effect removal step). The corner frequency of the events should not affect the results because the channel-wise spectral ratios remove the source effect. Also, the measured frequency band is higher than the corner frequency, as all events are less than magnitude 2, for which we expect the corner frequency < 20 Hz for a spectral stress drop

21699356, 2026, 9, Downloaded from https://agupubs.onlinelibrary.wiley.com/doi/10.1029/2026JB034276, Wiley Online Library on [23/10/2026]. See the Terms and Conditions (https://onlinelibrary.wiley.com/terms-and-conditions) on Wiley Online Library for rules of use; OA articles are governed by the applicable Creative Commons License

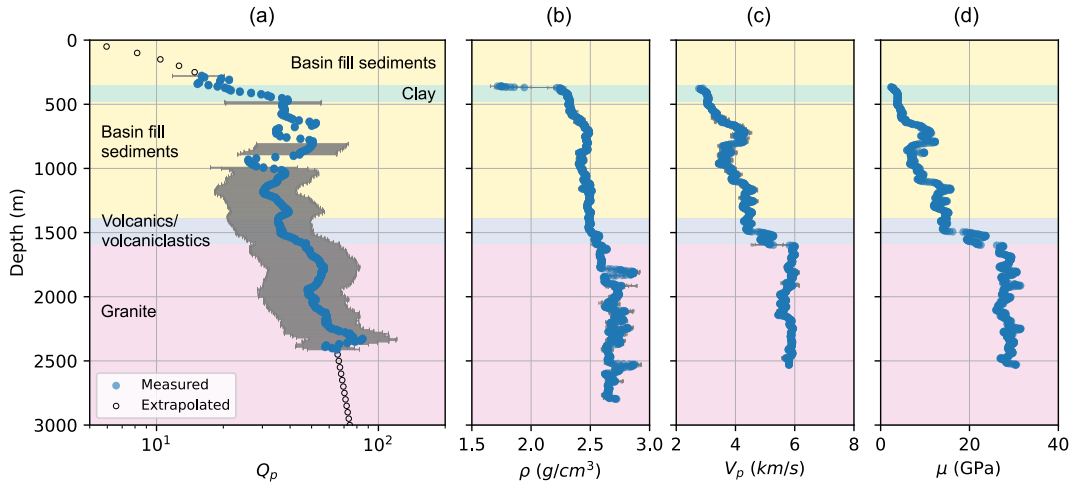


Figure 6. (a) Quality factor of the P wave (Q_p) from the attenuation analysis versus (b) density (ρ), (c) P-wave velocity (V_p), and (d) shear-modulus (μ) from the well log. Each blue dot is the median of measurements within 20 m. The error bars indicate median absolute deviations. We extrapolate the Q values (hollowed circles) for the source parameter analysis in Section 5. Shaded colors indicate geological formations (Fercho et al., 2024). (b) and (c) are from the well logs (Fercho et al., 2024). (d) is calculated from well-log shear-wave velocity and ρ.

>2 MPa. We only consider frequency-independent Q in this study, as the decay on the spectral ratios appears to fit Equation 6 well with a constant Q (Figure 5b).

Then, each channel has several Q measurements associated with the 20 m stacking and the 80-channels spectral division. We take the median Q and the median absolute deviation for error. We compare Q with density (ρ), P-wave velocity (V_p), and shear modulus (μ) from the well logs. We smooth the well log using a 20 m window by taking the median value and the median absolute deviation for each window.

We calculate the cumulated attenuation (κ) along the ray path using (Hough & Anderson, 1988):

$$\kappa = \int_{\text{path}} \frac{tt_i}{Q_i}, \tag{7}$$

where tt_i and Q_i are the travel time and Q inside each layer, respectively.

For structures shallower than 300 m, the high-frequency signal is lost to the combination of high attenuation and large gauge length effects due to the low velocity. We extrapolate shallow Q by assuming Q to continue the 100 m scale decreasing trend toward the near surface. For structures deeper than 2,450 m, no event with low incident angles is available. We extrapolate deep Q by assuming linearly increasing Q with depth, assuming $Q = 70$ at 2,700 m. This assumption is verified in Section 5.1.3, which shows no significant depth-dependence for corner frequency measured by models constrained by such a Q assumption for individual events.

4.1. Attenuation Structure

Figure 6 shows the resulting 1D Q profile compared with density, P-wave velocity, and shear modulus from the well logs. Above 500 m depth, the shallow basin fills and clay have low Q, ρ, and V_p. From 500 to 1,500 m, Q generally increases due to sediment compaction with small variations of sub-layers. The granite basement is at about 1,500 m depth with a sudden large increase in V_p and μ. Q and ρ also increase at the basement, but not as much as the velocity and the shear modulus. This is consistent with previous borehole studies in Parkfield (Jongmans & Malin, 1995), Cajon Pass in Southern California (Abercrombie, 1997), and Basel geothermal field in Switzerland (Bethmann et al., 2012) that found depth, rather than rock type, being the main factor affecting Q. Figure 7 shows the cumulative attenuation for an earthquake at 2,800 m depth and the general agreement with these previous borehole studies. The cumulative attenuation increases rapidly toward the near surface.

21699356, 2026, 9, Downloaded from https://agupubs.onlinelibrary.wiley.com/doi/10.1029/2026JB034276, Wiley Online Library on [23/10/2026]. See the Terms and Conditions (https://onlinelibrary.wiley.com/terms-and-conditions) on Wiley Online Library for rules of use; OA articles are governed by the applicable Creative Commons License

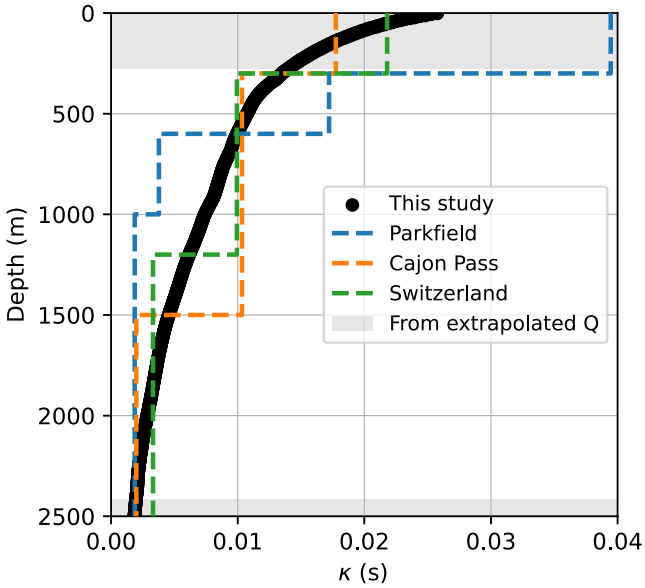


Figure 7. Cumulative attenuation (κ) (black curve) for an event at 2,800 m depth. Values in the gray area are estimated based on extrapolated Q. Dashed curves are previous studies: Jongmans and Malin (1995) (Parkfield), Abercrombie (1997) (Cajon Pass, Southern California), and (Bethmann et al., 2012) (Basel, Switzerland).

5. Earthquake Source Parameters

5.1. Individual Event Spectral-Modeling Approach

5.1.1. Theory

In this part, we model the strain-rate converted farfield displacement spectra ($\Omega(f)$) using the Brune source model (Boatwright, 1978, 1980; Brune, 1970) combined with exponential attenuation (Anderson & Hough, 1984):

$$\Omega(f) = \frac{\Omega_0}{\left[1 + \left(f/f_c\right)^{\gamma n}\right]^{1/\gamma}} \cdot e^{-\pi f \kappa}, \tag{8}$$

where Ω_0 is the amplitude at the low-frequency asymptote, f_c is the corner frequency, and $n = 2$ is the high-frequency fall-off rate. Using $\gamma = 1$ or 2 does not change our results significantly. We assume $\gamma = 1$ (Brune model), which gives a slightly better fit than $\gamma = 2$ (Boatwright model) after all quality control (Figure S2 in Supporting Information S1). κ is the high-frequency attenuation parameter (Equation 7).

The main problem with using such a single-spectrum approach is the large trade-off between the earthquake source parameters (Ω_0 and f_c) and the attenuation (e.g., Ko et al., 2012), which includes both a travel time component and a travel-time independent shallow site component (e.g., Ahn et al., 2025; Chang et al., 2025). Here we fix the attenuation using the Q structure obtained above, and assume a gently increasing Q for depth between the earthquake and the deepest station. We will analyze the channel dependence of the results to check potential trade-offs and compare with the EGF approach to examine the Q assumption.

We calculate the seismic moment of each earthquake from the Ω_0 values using (Brune, 1970):

$$M_0 = \frac{4\pi\rho c^3 R \Omega_0}{U_{\phi\theta}}, \tag{9}$$

in which $\rho = 2{,}790$ kg/m^3 is the density, c is the P-wave velocity at the hypocenter, R is the hypocentral distance that accounts for geometrical spreading, and $U_{\phi\theta} = 0.52$ is the mean radiation pattern coefficient for P waves (Madariaga, 1976). We calculate moment magnitude using (Hanks & Kanamori, 1979)

$$M_w = \frac{2}{3}\log_{10} M_0 - 6.07. \tag{10}$$

5.1.2. Data Processing and Quality Control for Single Spectral Approach

We calculate P-wave spectra using a 0.1 s time window with the same processing (demeaning in space and time, detrending in time, tapering in time) and quality control (spectral point-wise SNR > 3) procedures in Section 4. The 0.1 s window is chosen to avoid contamination of other phases, based on Abercrombie et al. (2016), which is 10 times larger than the source duration of most events with $f_c > 100$ Hz. To check if the window causes biases to the larger events, expected to have $f_c < 100$ Hz, we also test using a 0.2 s window. We get similar stress drop results for the larger events, but lower M_w and higher f_c for some of the smaller events (see Text S2 in Supporting Information S1), suggesting our choice of window is not causing significant bias, similar to the results of Ide et al. (2003) (their Figure A2). We require the S wave to arrive after the selected P wave window. We consider the flat response (R_1) and convert the strain rate to displacement (Equations 3 and 4). We remove the gauge length effect by dividing R_2. Finally, we resample the spectra with constant spacing in the log-frequency space and keep the spectra between 10 and 400 Hz. We stack the displacement spectra by taking the median amplitude at a frequency among 20 m of channels, which slightly improves the amplitude stability, especially at the edges of the frequency range where the SNR is the lowest (Figure S3 in Supporting Information S1). Figure 8 shows the stacked displacement spectra. We take the median channel location and incident angle for each stack. We only

21699356, 2026, 9, Downloaded from https://agupubs.onlinelibrary.wiley.com/doi/10.1029/2026JB034276, Wiley Online Library on [23/10/2026]. See the Terms and Conditions (https://onlinelibrary.wiley.com/terms-and-conditions) on Wiley Online Library for rules of use; OA articles are governed by the applicable Creative Commons License

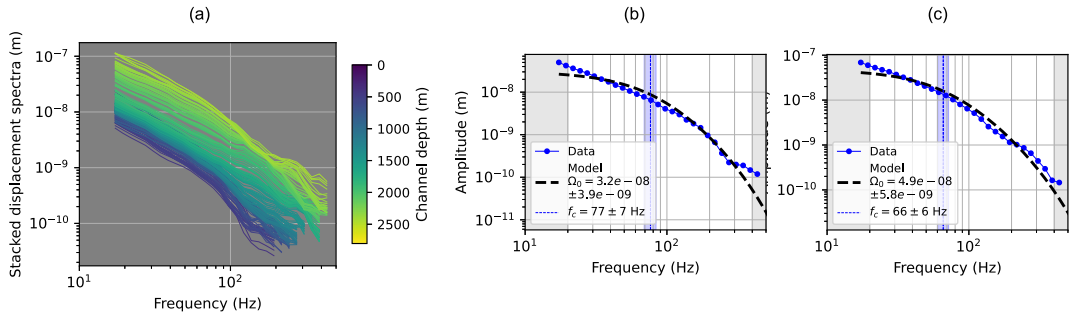


Figure 8. (a) Response-corrected stacked P-wave displacement spectra for Event 1 (catalog M_w 1.5) and two single spectral modeling examples (a) at 2,139 m depth and (c) at 2,323 m depth. Each spectral point is the median of 10 close channels (which spans 20 m along the cable), where each individual spectrum of a channel has been through the point-wise SNR > 3 quality control, removed the gauge length and flat responses, and resampled in the log-frequency domain. We fit the Brune model with estimated attenuation (black dashed) (Equation 8) to the stack spectra (blue) to determine the corner frequency (f_c) (vertical line) and low-frequency amplitude (Ω_0). The white part inside the gray shades indicates the fitting range (20–400 Hz). The blue shade is the standard deviation. When determining the median f_c and Ω_0 for an event, we only include channels between 1,800 and 2,400 m depth, which have lower misfits, and channels with incident angle <45° to reduce response-correction-related bias.

retain stacks with median incident angle <45° to avoid response-correction related bias. Note that this criterion is more generous than the <30° limit used for the attenuation analysis in Section 4. When measuring Q, we want the wave to travel in mostly the vertical direction, while here, we want to reduce the range of possible responses to reduce correction bias. We estimate cumulative attenuation using Equation 7 for each stack. We use ray-tracing to estimate the travel time spent in each Q layer for the cumulative attenuation between each channel stack and source pair.

We use a least-squares approach (Newville et al., 2016) to fit Equation 8 to the stacked displacement spectra to resolve f_c and Ω_0 (Figures 8b and 8c). We minimize the model misfit between $f_{\min} = 20$ Hz (2 times 1/time window) and $f_{\max} = 400$ Hz (0.8 times the Nyquist). Using a different frequency range does not change the results significantly (e.g., 60–400 Hz; Figure S4 in Supporting Information S1). We remove results with large misfits (reduced chi-square >0.02), large uncertainty (standard deviation >50% of the results), or f_c that are too close to the edges (>0.8 $f_{\max}$ or <1.2 $f_{\min}$). We select a channel depth range for our analysis of 1,800–2,400 m. We prefer this range because they have more low-misfit measurements (Figure S5 in Supporting Information S1). Shallower channels suffer from the difficulty in separating a reflected phase at the basement (1,500 m depth). High attenuation and lower medium velocity also severely limit the available bandwidth at shallower depths (blue spectra in Figure 8a).

The f_c and Ω_0 measurements for each event form a distribution that has a central value (Figure S6 in Supporting Information S1). We take the median f_c and Ω_0 as the final results. We convert Ω_0 to moment magnitude (Equations 9 and 10) and estimate source radius, slip, and spectral stress drop (Equations 12–14).

5.1.3. Channel Dependence

We check the consistency of measurements between channels to ensure no significant biases are involved. Figure 9 shows how individual single spectral fitting measurements deviate from the final result. We divide all M_w and f_c measurements on the individual stacked spectrum at different channel depths by the final results of the events. Note that we include only M_w and f_c measurements that pass the quality control here. The majority of the measurement (yellow) at individual channel depth aligns with the final results ($M_w/M_{w,\text{event}}$ and $f_c/f_{c,\text{event}} = 1$), which ensures the measurement consistency. The corner frequency has a slight channel depth dependence where shallower channels tend to have higher f_c measurements (i.e., $f_c/f_{c,\text{event}} > 1$).

This channel dependence can result from uncertainty in response correction, which can cause trade-offs with corner frequency and seismic moment in the Brune model. Inaccuracy in incident angle and apparent velocity can systematically bias gauge length and flat response estimates between stacks of channels (Equations 2 and 5). Hence, if we include measurements of a large range of incident angles, we cannot tell if the observed source

21699356, 2026, 9, Downloaded from https://agupubs.onlinelibrary.wiley.com/doi/10.1029/2026JB034276, Wiley Online Library on [23/10/2026]. See the Terms and Conditions (https://onlinelibrary.wiley.com/terms-and-conditions) on Wiley Online Library for rules of use; OA articles are governed by the applicable Creative Commons License

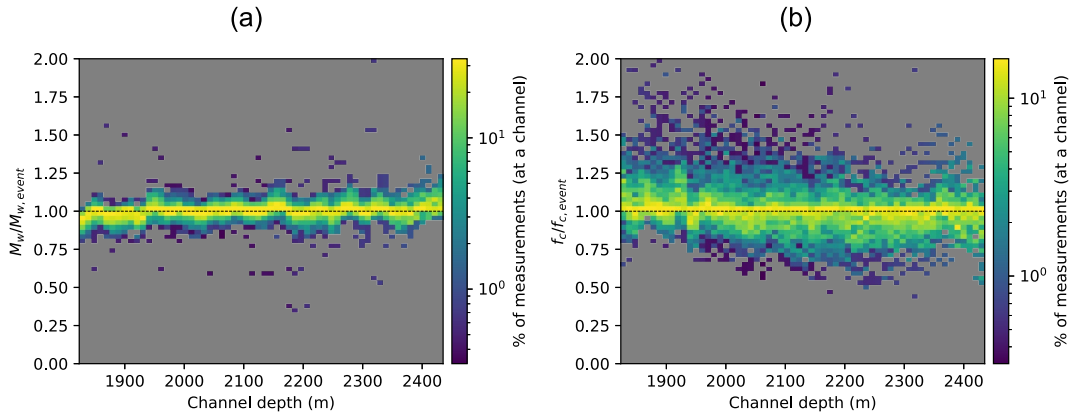


Figure 9. Variation of (a) moment magnitude (M_w) and (b) corner frequency (f_c) measurements along the cable in the single spectrum approach. The *x*-axis is the channel depth to which the stacked spectra belong. The *y*-axis reports all single spectral fitting measurements that pass the quality control (Section 5.1.2) divided by the final result (which is the median of channel measurements) of the events. The color indicates the percentage of measurements at a given channel.

parameter variation is real or due to biases in response removal. Thus, we limit the incident angle to be less than 45°. If we include a larger range of incident angles, the depth dependence increases, and we risk having more biases (Figure S7 in Supporting Information S1).

Uncertainty in Q can also result in over- or under-correcting attenuation that can cause trade-offs with f_c (e.g., Ahn et al., 2025; Ko et al., 2012; Shearer et al., 2025). If we use a larger Q, we get larger channel dependence for f_c, which signals potential trade-offs between f_c and Q (Figure S8 in Supporting Information S1).

5.2. Verification of f_c Using Empirical Green's Function Approach

5.2.1. Theory

Given the large uncertainties in estimating small earthquake source parameters (e.g., Abercrombie, 2021), it is advisable to test whether other approaches result in similar estimates (e.g., Abercrombie et al., 2025; Ruhl et al., 2023). The EGF method (Hartzell, 1978; Hough, 1997) uses a collocated small event, with a similar focal mechanism, as an EGF. The spectral ratio of a target and an appropriate EGF event pair can isolate the source terms without the need to model either the wave propagation effects or the directivity/unit-conversion/instrument responses. However, the approach does need appropriate pairs of events, both with a wide frequency range of signal above noise, to work well (Abercrombie, 2015). We find two good-quality event pairs and use them to validate the estimates of f_c from the single spectral method.

We model the spectral ratio as:

$$\Omega_r(f) = \Omega_{0r}\left[\frac{1+(f/f_{c2})^{\gamma n}}{1+(f/f_{c1})^{\gamma n}}\right]^{1/\gamma}, \tag{11}$$

Ω_{0r} is the relatively low-frequency amplitude of the event pair. f_{c1} and f_{c2} are the corner frequencies of the target and the EGF events, respectively. Following the results of the single spectral analysis, we assume $\gamma = 1$ and $n = 2$.

5.2.2. Data Processing and Quality Control for EGF Approach

We first find event pairs whose mutual distances are <100 m (location uncertainty) (Pairs 1 and 2). We require the low-frequency amplitude ratio >2 and the magnitude difference >1.0 to allow proper determination of f_{c1} (Abercrombie, 2014, 2015). We align the P arrivals of the event pair in time by finding the maximum cross correlation and cut the 0.2 s P arrival window. We require a cross-correlation coefficient (cc) >0.8 between the target and EGF events' DAS raw waveforms filtered between 5 and 50 Hz (Abercrombie, 2015; Pennington

21699356, 2026, 9, Downloaded from https://agupubs.onlinelibrary.wiley.com/doi/10.1029/2026JB034276, Wiley Online Library on [23/10/2026]. See the Terms and Conditions (https://onlinelibrary.wiley.com/terms-and-conditions) on Wiley Online Library for rules of use; OA articles are governed by the applicable Creative Commons License

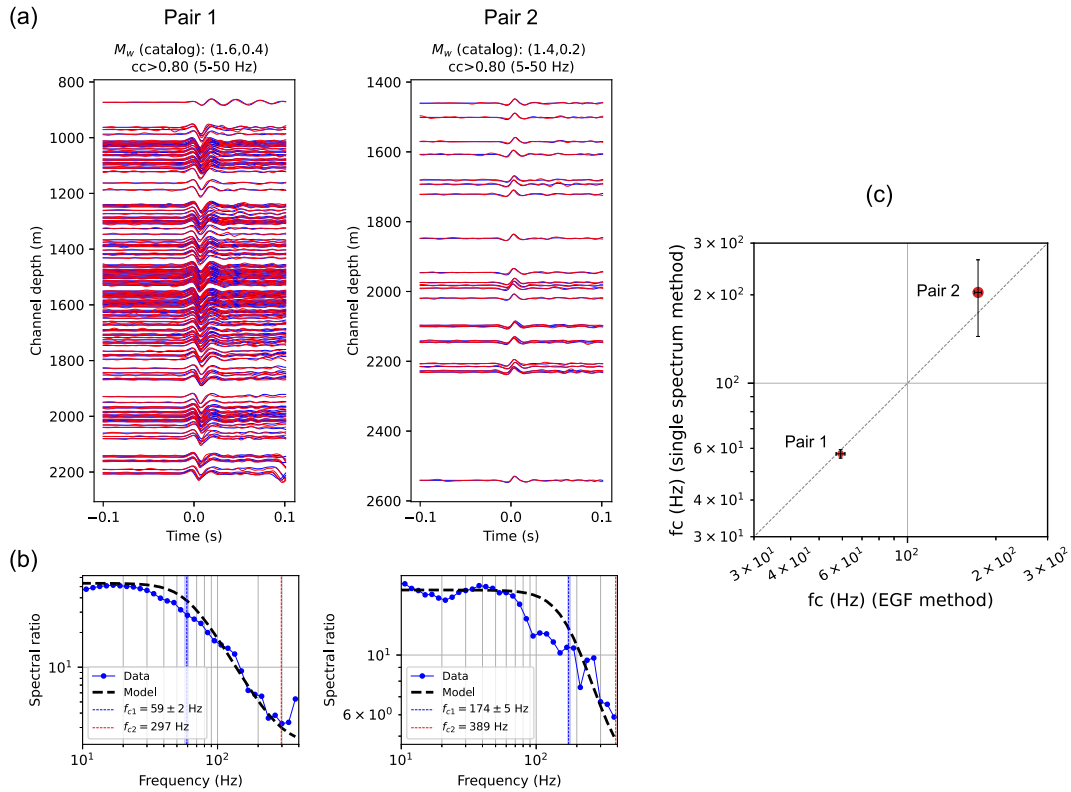


Figure 10. Spectral ratio analysis using Empirical Green's Function (EGF). (a) Aligned P-wave waveforms (normalized) of two target (blue) and EGF (red) event pairs (Pairs 1 and 2), filtered between 5 and 50 Hz. (b) Stacked spectral ratio and the best-fitted model. Pairs 1 and 2 stack 277 and 43 available channels, respectively. Target corner frequency (f_{c1}) and standard deviation are the vertical blue line and shade. EGF corner frequency (vertical red line) is fixed, assuming a constant spectral stress drop. The individual channel spectrum used for calculating the spectral ratios has passed the point-wise SNR > 3 quality control and has been resampled in the log-frequency domain. (c) Comparison of the corner frequency estimated by the spectral ratio and single spectral results. The gray dashed line is 1:1. The error bars for the single spectral results are the standard deviation of all channel group measurements. The errorbar for the spectral ratio is the standard deviation of the fitting. The size of the dots is inversely proportional to the misfit of the spectral ratio fitting. We require a cross-correlation coefficient $cc > 0.8$.

et al., 2022) (Figure 10a). Note that this bandpass filter is only for calculating cc below expected corner frequencies, and we do not filter the waveforms used in the later spectral fitting. Another quality control procedure is similar to Section 5.1.2, but no response removal is needed. We divide the raw, recorded strain rate spectra of the target event by those of the EGF. We resample the spectral ratios to equal spacing in the log-frequency domain. Then, we stack all ratios.

We fit the stacked spectral ratios with Equation 11 to resolve Ω_{0r} and f_{c1} (Figure 10b). To avoid trade-offs between f_{c1} and f_{c2} (Shearer et al., 2019), we fix f_{c2} assuming a constant spectral stress drop of 37 MPa (median of the single spectral method results). We require $f_{c1} < 0.6 f_{c2}$ for proper determination of f_{c1}. We discard results with large misfits (reduced chi-square >0.005).

We only find two well-recorded event pairs that meet the quality criteria we impose to obtain reliable corner frequency f_{c1} estimates for comparison with the single spectral f_c results (Figure 10c). The corner frequencies estimated by the two approaches are consistent and within the error bars (fitting standard deviation). f_c of event 1 is 59 ± 2 Hz using EGF and 57 ± 2 Hz using single spectral method. f_c of event 2 is 175 ± 5 Hz using EGF and 203 ± 65 Hz using single spectral method. This comparison implies that there are no large systematic biases due to parameter trade-offs in the single spectral approach for these two events.

21699356, 2026, 9, Downloaded from https://agupubs.onlinelibrary.wiley.com/doi/10.1029/2026JB034276, Wiley Online Library on [23/10/2026]. See the Terms and Conditions (https://onlinelibrary.wiley.com/terms-and-conditions) on Wiley Online Library for rules of use; OA articles are governed by the applicable Creative Commons License

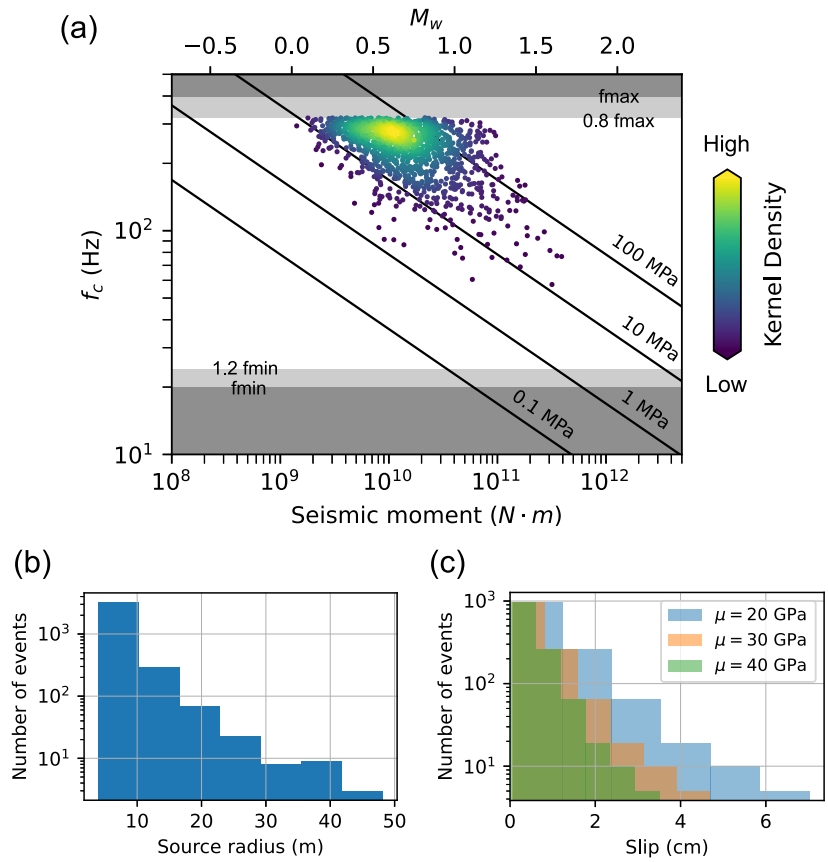


Figure 11. Source parameter results. (a) Corner frequency (f_c) versus seismic moment and moment magnitudes (M_w). Constant spectral stress drop ($\Delta\sigma$) values are marked by the black lines. Each point is the median of the channels. The color indicates the kernel density of data points. Error bars are the median absolute deviation. We minimize model misfit between 20 Hz ($f_{\min}$) and 400 Hz ($f_{\max}$) (bounded by the dark gray shades). We only retain f_c measurements that lie between $1.2\,f_{\min}$ and $0.8\,f_{\max}$ (bounded by the light gray shades). (b) Source radius. (c) Source slips assuming shear modulus (μ) = 20, 30, 40 GPa. There are more small-radius, slow slip events.

5.3. Radius, Slip, and Spectral Stress Drop

For a circular crack, the source radius (r) can be estimated following Brune (1970), and Madariaga (1976):

$$r = k\beta/f_c, \tag{12}$$

in which k is a constant that depends on the theoretical rupture model and β is the S-wave velocity at the hypocenter. We assume $k = 0.38$ from (Kaneko & Shearer, 2015). From the definition of seismic moment, the average slip of a circular source D is (Aki & Richards, 2002):

$$D = \frac{M_0}{\pi\mu r^2}. \tag{13}$$

The granite basement has μ = 25–30 GPa (Figure 6d). We estimate the slip with μ = 20, 30, and 40 GPa to understand how the slip might vary given a shift in μ.

The spectral stress drop can then be estimated following (Brune, 1970; Eshelby, 1957; Madariaga, 1976):

$$\Delta\sigma = \frac{7}{16}\frac{M_0}{r^3}. \tag{14}$$

21699356, 2026, 9, Downloaded from https://agupubs.onlinelibrary.wiley.com/doi/10.1029/2026JB034276, Wiley Online Library on [23/10/2026]. See the Terms and Conditions (https://onlinelibrary.wiley.com/terms-and-conditions) on Wiley Online Library for rules of use; OA articles are governed by the applicable Creative Commons License

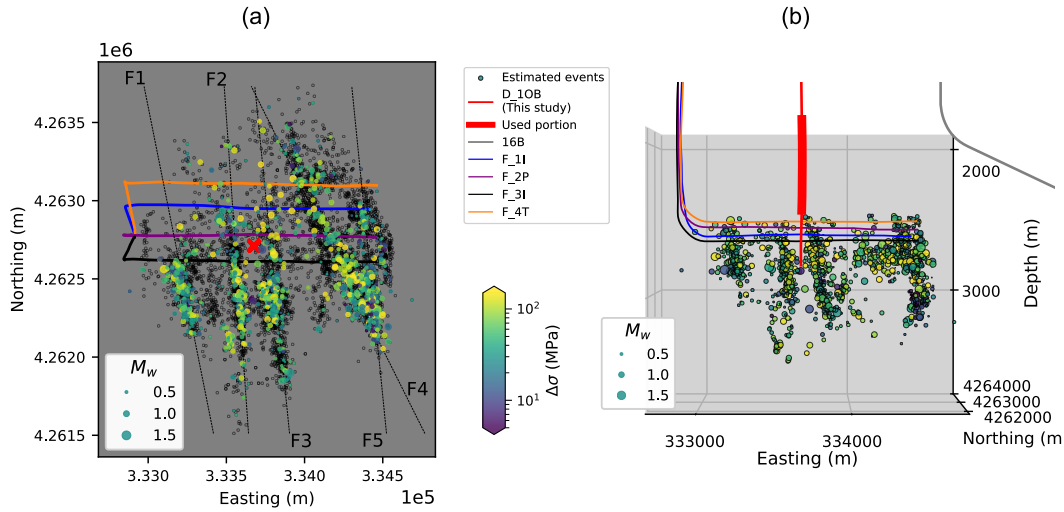


Figure 12. Spectral stress drop distribution in (a) 2D and (b) 3D. Earthquakes with successful spectral stress drop are illustrated by color points (marker size proportional to moment magnitude). Gray dots are other events (same marker size). See cross-section views along faults F1–F5 in Figure 13. The x, y, z axes are 1:1:1.

5.4. Earthquake Source Parameter Results

Figure 11a shows the spectral stress drop, magnitude, and corner frequency results from the single spectral approach. Most spectral stress drops fall between 5 and 130 MPa, with the highest event density centering at 37 MPa. The absolute values fall within the typical ranges estimated for spectral stress drop for earthquakes over a very wide magnitude range (e.g., Baltay et al., 2024). Community-wide work on improving spectral stress drop estimates has shown that the relative variation between events is much better resolved than the absolute values (Abercrombie & Baltay, 2025; Abercrombie et al., 2025). The distribution of spectral stress drop is impacted by $f_{\max}$, and our results exclude or underestimate spectral stress drops for some events below $M_w \sim 1$. The spectral stress drops generally exhibit a constant range across magnitudes, without an obvious scaling relation with seismic moment. We have a limited magnitude range ($0 < M_w < 1.7$), so it might be difficult to distinguish any localized breakdown in self-similarity. To analyze events with lower magnitudes ($M_w < 0$), both a higher sampling rate and sufficient high-frequency signal above the background noise are required.

The moment magnitude is consistent with independent estimates of magnitude using surface geophones and seismometers, by time-domain integration of P or S waves, provided by a vendor (Figure S9 in Supporting Information S1; cross-correlation coefficient = 0.6, mean M_w difference = 0.1 from a T-test). We note that the vendor-provided magnitudes are preliminary estimates based on personal communication with Fervo Energy, and future work is required to make a proper comparison using more sophisticated processing flows. The surface sensors cannot calculate f_c because of insufficient SNR above 100 Hz (Figure S10 in Supporting Information S1).

The source radius follows a power law distribution (Figure 11b), which is consistent with the magnitude-invariant spectral stress drop based on Equation 14. Half of the events have a radius less than 15 m, whereas the largest event reaches 45 m. Assuming the simple source model, a constant rupture velocity, and a shear modulus of 30 GPa, the average seismic slip in the majority of events is approximately 0.5–5 cm (Figure 11c). Like the source radii and the spectral stress drop estimates, these numbers will vary with varying temperature or shear modulus, or the assumption of the source model.

Figure 12 shows the distribution of the spectral stress drop value we obtain. We separate the clusters into 5 vertical fracture planes (F1–F5). Spectral stress drops on F1–F3 show that small-scale variability dominates with no obvious spatial pattern (Figures 13a–13c). Such relatively small-scale variability is observed in most studies of earthquake sequences (few to tens of km; Abercrombie & Baltay, 2025; Abercrombie et al., 2016; Kaneko & Shearer, 2014; Ruhl et al., 2023; Vandevert et al., 2025; Yu et al., 2020). There is a lower spectral stress drop cluster (Figures 13d and 13e) at the intersection of F4 and F5 on the southeast corner, possibly reflecting a damage zone at the fault intersection. There are also some higher spectral stress drop zones, such as the cluster between 2,700–2,900 m on F4, surrounded by a smaller stress drop area, possibly showing fault heterogeneity. In the later

21699356, 2026, 9, Downloaded from https://agupubs.onlinelibrary.wiley.com/doi/10.1029/2026JB034276, Wiley Online Library on [23/10/2026]. See the Terms and Conditions (https://onlinelibrary.wiley.com/terms-and-conditions) on Wiley Online Library for rules of use; OA articles are governed by the applicable Creative Commons License

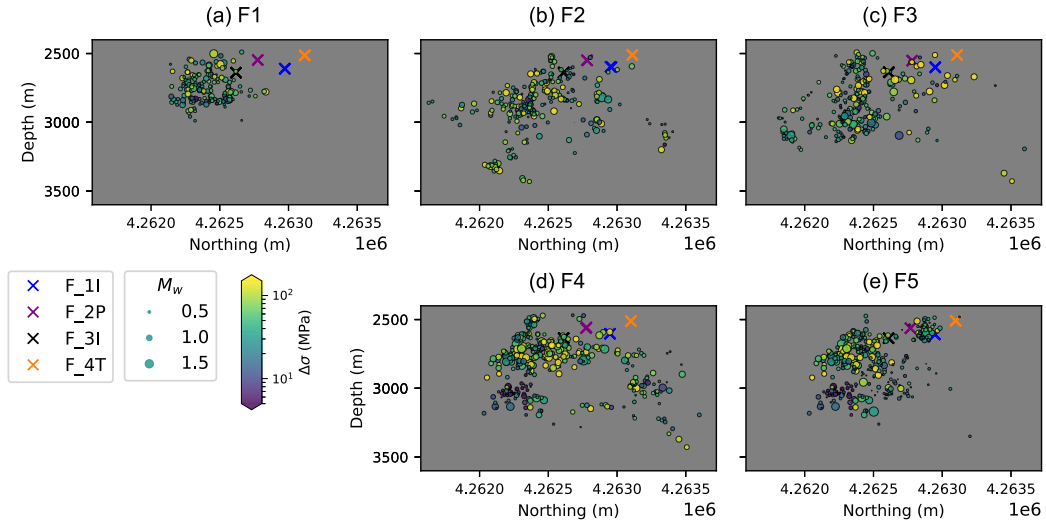


Figure 13. Vertical cross-section depicting spectral stress drop distribution along faults F1–F5 (a–e). Events within 100 m of the fault line are plotted. The crosses are the injection wells. The horizontal and vertical axes are 1:1.

discussion, we discuss several potential factors that might affect the observed spectral stress drop, including observational errors, pore pressure, stress condition, or fault heterogeneity.

We investigate whether the spectral stress drop estimates show any clear pattern of dependence on fault stress by checking whether they correlate with fault orientation, depth, or adjacency to fluid injection. We compare the spectral stress drop with the focal mechanisms calculated by Mohammadi et al. (2025), but find no significant relationship (Figure 14a), consistent with the work of Ruhl et al. (2023). We observe a decrease in spectral stress drop from 44 MPa at 2,500 m to 25 MPa at 3,000 m, then an corresponding increase beneath 3,000 m (to 65 MPa, but with fewer measurements) (Figure 14b), suggesting increase in normal stress with depth is not a major factor, but perhaps suggesting a dependence on higher attenuation or a changes in fault complexity near 3,000 m depth. A decrease in stress drop in proximity to the injection site (a few km) has been observed in previous studies (Goertz-Allmann & Wiemer, 2013; Yu et al., 2020), but if anything, we see the opposite trend (Figure 14c), where spectral stress drop decreases from 44 MPa at 50 m to 36 MPa at 500 m. This may simply reflect the depth dependence noted earlier.

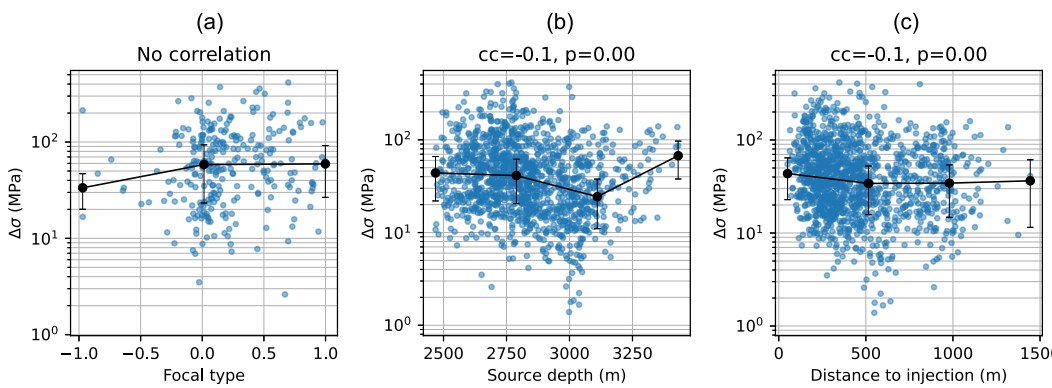


Figure 14. Spectral stress drop versus (a) focal mechanism from Mohammadi et al. (2025), (b) source depth, and (c) distance between source and the injection. Focal type in (a) is calculated following Shearer et al. (2006), where −1, 0, and 1 represent normal, strike-slip, and reverse faulting, respectively. *cc* is the cross-correlation coefficient. We assume a *p*-value <0.05 is statistically significant; otherwise, no correlation. The black curves are the median of the binned values. The bin width in each subplot is $\pm x/2$ around the black dots, with x being the horizontal distance between the equally spaced black dots. The error bar shows the median absolute deviation.

21699356, 2026, 9, Downloaded from https://agupubs.onlinelibrary.wiley.com/doi/10.1029/2026JB034276, Wiley Online Library on [23/10/2026]. See the Terms and Conditions (https://onlinelibrary.wiley.com/terms-and-conditions) on Wiley Online Library for rules of use; OA articles are governed by the applicable Creative Commons License

21699356, 2026, 9, Downloaded from https://agupubs.onlinelibrary.wiley.com/doi/10.1029/2026JB034276, Wiley Online Library on [23/10/2026]. See the Terms and Conditions (https://onlinelibrary.wiley.com/terms-and-conditions) on Wiley Online Library for rules of use; OA articles are governed by the applicable Creative Commons License

6. Discussion

6.1. A High-Resolution Q Structure

To our knowledge, this is the first high-resolution Q structure for the upper 2,500 m crust from seismic observations. The Q is very low in the near-surface 400 m ($Q < 30$) (Figure 6). Q increases mainly with depth. At the granite basement, Q slightly increases, but the increase is not as strong as the velocity increase at the lithological boundary. The results agree with previous borehole studies in California (Abercrombie, 1997, 1998; Jongmans & Malin, 1995) and Switzerland (Bethmann et al., 2012). They found $Q < 30$ in the top 500 m. They also found that shallow attenuation is more affected by depth and overburden than by rock types. Our attenuation results emphasize the importance of considering shallow attenuation when determining the shape of the source spectra at high frequencies (Abercrombie, 1997; Abercrombie et al., 2025; Ahn et al., 2025; Chang et al., 2025; Shearer et al., 2025; Strumia et al., 2024). More attenuation analysis using borehole or horizontally deployed DAS (e.g., Strumia et al., 2024), possibly on different seismic phases, would provide new constraints for the attenuation in the crust and improve other seismic applications, including source and site effect studies and earthquake hazard analysis.

6.2. The Value of Understanding Shallow Attenuation for Source Parameter Analysis

Our spectral stress drop results lie well within the large range of typical observed stress drops from the community study (Abercrombie et al., 2025; Baltay et al., 2024). The community study found spectral stress drop estimated using different methods can span over six orders of magnitudes (0.001 to over a few thousands MPa), while the apparent trend of magnitude-dependent stress drop likely reflects between-method discrepancies (Abercrombie et al., 2025) and different attenuation corrections (Shearer et al., 2025), in particular, depth-dependent (Abercrombie et al., 2021) and site-dependent attenuation (Ahn et al., 2025; Chang et al., 2025). The spectral stress drop scattering due to different methods and attenuation assumptions is much greater than any systematic difference between induced and tectonic events (Abercrombie et al., 2025; Baltay et al., 2024). Here, the downhole DAS provides a good way to quantify shallow attenuation for source parameter estimates. More future studies using similar methods will help direct comparison of absolute or relative spectral stress drop between induced and tectonic events.

6.3. Effects of DAS Response Correction on Spectral Analysis

The DAS cable directivity and gauge length effects need to be considered for spectral analysis. However, it is difficult to completely correct all DAS responses because accurate correction depends on the uncertainty of location and velocity (Equations 2 and 5). Hence, it is important to recognize how sensitive the analyses are to the responses.

The Q results do not change significantly considering the gauge length effect or not (Figure S11 in Supporting Information S1). This is probably because the gauge length effect is less prominent below 100 Hz (Figure 4c) and has less influence on the frequency-independent Q we measure between 20–200 Hz.

The source parameters are more sensitive to the response correction. The magnitude depends on the low-frequency amplitude and hence is affected mostly by the flat response (Figure 4b). Having a smaller incident angle (for P waves) is advantageous when measuring M_0 as the amplitude needs less correction. The corner frequency is estimated from the amplitude drop-off on the spectra, which is affected the most by the gauge length (Figure 4c). Hence, a small gauge length and a higher incident angle (for P waves) are preferred when measuring f_c. In this study, we limit the range of incident angle to be less than 45° for estimating source parameters. This reduces potential biases due to uncorrected or overcorrected responses. We also use reliable EGF estimates to verify that no large bias is present in the corner frequency.

In this study, the limitation on characterizing f_c of low magnitude events comes from low SNR at high frequency due to not only background noise but also the gauge length effect, which poses an amplitude notch (Figure 4c). The amplitude notch is less of a concern for deep borehole cables because the apparent velocity is higher (high medium velocity and/or large incident angle) and the amplitude cutoff is above the Nyquist frequency. Shallow cables (~100 m) are severely limited by the gauge length effect for spectral modeling at tens or hundreds of Hz because of the lower apparent velocity (Abukrat et al., 2023). Lowering gauge length is a possible solution for using shallow cables, but a small gauge length suffers a lower SNR (Hartog, 2017). With advances in the DAS

21699356, 2026, 9, Downloaded from https://agupubs.onlinelibrary.wiley.com/doi/10.1029/2026JB034276, Wiley Online Library on [23/10/2026]. See the Terms and Conditions (https://onlinelibrary.wiley.com/terms-and-conditions) on Wiley Online Library for rules of use; OA articles are governed by the applicable Creative Commons License

interrogator, this can be improved in the future. We also need to use a higher sampling rate >1000 Hz for small events.

Here, we do not consider the DAS amplitude saturation effect, as no amplitude clipping is observed in our data. For larger magnitude events, larger gauge length, or slower pulsing rate of the interrogator, the amplitude might clip because of cycle skipping of the phase shift measurement. We refer readers to Zhai et al. (2025) and van den Ende et al. (2025) for the amplitude saturation issue of DAS.

6.4. Potential Uncertainty and Biases in Source Parameters

Although we try to minimize response and attenuation-related biases by comparing with EGF approach and reducing measurement channel depth dependence, biases might still exist as (a) we only find two EGF pairs to compare with, and (b) the assumption that f_c should be consistent across channels might be incorrect considering source directivity (Kaneko & Shearer, 2014). If we do not remove gauge length response, we obtain systematically smaller f_c and the median stress drop decreases to 29 MPa (Figures S12 and S13 in Supporting Information S1). If we assume a lower attenuation (interpolate Q below 2,450 m, assuming $Q = 100$ instead of $Q = 70$ at 2,700 m), we also obtain smaller f_c and a smaller median spectral stress drop of 22 MPa (Figures S14 and S15 in Supporting Information S1). However, the general trend of constant spectral stress drop does not change in either case. We encourage future studies with more available EGF pairs and deeper Q information to further investigate microearthquake stress drops.

Source model variation and model misfits due to complex ruptures not captured by the simple model can cause apparent scattering in spectral stress drop. We assume a simple circular crack with instantaneous rupture and a ω^{-2} ($n = 2$) model. However, the events might deviate from this classic scenario, for example, having different source geometry, rupture directivity, rupture speed, rupture mode, and spectral fall-off rate (Madariaga, 1976; Kaneko & Shearer, 2015; Y. Wang & Day, 2017; Vandevert et al., 2025; Mosconi et al., 2026). A lower f_c for P waves might indicate that rupture speed is slower or n is higher than assumed (Kaneko & Shearer, 2015). While classic crack-like rupture has been observed to follow $n = 2$, pulse-like or self-arresting rupture can have less high-frequency energy and a larger n (Mosconi et al., 2026), and potentially multiple f_c (Y. Wang & Day, 2017). Vandevert et al. (2025) found assuming $n = 2$ produces higher $\Delta\sigma$ than assuming $n = 1.7$ for events of the same magnitudes. Trying to fit the complex sources with the simple model, the misfit might result in scattering apparent f_c and spectral stress drop. On the other hand, more complex ruptures can produce higher-frequency radiation but less total slip, which can look like high stress drops when it is not (Calderoni & Abercrombie, 2023; Lee et al., 2025).

6.5. Physical Implications of the Source Parameter Variability

Moving beyond potential observational error, variability in corner frequency and spectral stress drop might indicate different pore pressures, stress conditions, and fault heterogeneity. We discuss these factors below.

Changes in pore pressure have been found to be the main mechanism for injection-induced earthquakes (Moein et al., 2023). Elevated pore pressure reduces the effective normal stress and reduces stress drop (Shapiro & Dinske, 2021). Also, the poroelastic stress perturbation might cause less critically stressed faults to fail near the injection point (Goertz-Allmann & Wiemer, 2013). Both changes in pore pressure and poroelastic stress can cause the stress drop to increase with distance to injection. However, we do not observe such a trend (Figure 14c); although we note that it might be difficult to observe such a trend as the events contain multi-stage injection effects.

Fault roughness and maturity have been hypothesized to affect earthquake stress drop, with events on a smoother and more mature fault potentially having higher stress drop (Candela et al., 2011; Zielke et al., 2017). Repeated ruptures on the same fault patch can reduce fault roughness (L. Wang et al., 2024) and cohesion (Shapiro & Dinske, 2021), both of which increase stress drop over time. However, we do not observe an obvious temporal stress drop pattern on the faults (Figure S16 in Supporting Information S1). Hence, the temporal fault smoothing effect is not significant in the short time scale of 2–3 weeks. On the other hand, fault heterogeneity can result in variability of stress drop among subfault patches (Madariaga, 1979). The asperities that have higher strength and higher stress build-up can produce a concentrated large stress drop on the fault (Dreger et al., 2007). Previous studies have observed high static stress drop on identified asperities surrounded by small negative stress drop

areas (e.g., Asano & Iwata, 2011). This might also explain some of the high stress drop values we observed. Local damage zones might show lower spectral stress drop (Moyer et al., 2018), such as the intersection between F4 and F5 (Figures 13d and 13e).

7. Conclusion

We used DAS in a ∼3,000 m deep vertical borehole in the Cape Modern geothermal field to analyze attenuation and characterize microearthquakes during a geothermal stimulation. Borehole DAS forms an unprecedentedly dense array that we use to characterize crustal attenuation structure and obtain in situ measurements of small events.

Using the along-depth spectral ratio, we obtain a frequency-independent Q profile for P waves (Figure 6a). This is the first high-resolution Q structure in the upper 2,500 m of the crust obtained from seismic observations. We find low Q at the near surface ($Q < 30$ in the upper 400 m), and that attenuation decreases mainly with depth instead of depending on rock types, both of which agree with previous borehole studies in Parkfield (Jongmans & Malin, 1995), Cajon Pass (Abercrombie, 1997), and Switzerland (Bethmann et al., 2012). The cumulative attenuation is consistent with these studies (Figure 7). The high attenuation at the near-surface emphasizes the importance of considering shallow attenuation structure in source studies and ground motion analysis.

We estimate source parameters using a single spectral modeling approach. We directly model the DAS responses, including directivity, unit conversion, and the gauge length effect. We also model attenuation using the Q profile we obtained. We successfully resolved moment magnitude (M_w 0–1.7), corner frequency, source radius, slip, and spectral stress drop. The large variability of our spectral stress drop results is consistent with that seen in most previous studies (Abercrombie & Baltay, 2025; Abercrombie et al., 2016). Although some is likely an artifact of the simplified modeling and related uncertainties, our analysis suggests spatial heterogeneity in fault stress is perhaps the most likely cause, with pore pressure, pore-elastic stress, and temporal smoothing effects playing less important roles. The spectral stress drop shows no dependence on magnitude between M_w 0 and 1.7 (Figure 11a), showing no evidence of a characteristic nucleation size in this limited magnitude range.

The channel-dependent DAS responses can introduce additional biases if not accounted for properly. Removing the response can be difficult as it depends on the accuracy in location and velocity (Equations 2 and 5). One way to reduce response-related biases for analyzing spectral amplitude is to use cables with similar responses. Here, we limit the incident angle (<45°) in single-spectral source parameter calculation to reduce the range of response correction. We examine the measurement consistency between channels to check potential biases (Figure 9). We also use two event pairs with good Empirical Green's Functions to benchmark (Figure 10).

We demonstrate that downhole cables have great potential for studying crustal attenuation, which will help us understand earthquake observations. Future work includes investigating the Q structure at different locations and for more seismic phases. There is also a need for more microearthquake source parameter studies using DAS to facilitate comparison between different tectonic settings and between induced and tectonic events.

Acronyms

DAS	Distributed Acoustic Sensing
EGF	Empirical Green's Function
EGS	Enhanced Geothermal System
Q	Quality Factor
SNR	Signal-to-Noise Ratio

Conflict of Interest

The authors declare no conflicts of interest relevant to this study.

21699356, 2026, 9, Downloaded from https://agupubs.onlinelibrary.wiley.com/doi/10.1029/2026JB034276, Wiley Online Library on [23/10/2026]. See the Terms and Conditions (https://onlinelibrary.wiley.com/terms-and-conditions) on Wiley Online Library for rules of use; OA articles are governed by the applicable Creative Commons License

Availability Statement

The Supporting Information S1 files, including the source parameter, Q results, and DAS P-wave raw spectra of the events, are available at the Geothermal Data Repository (Chang et al., 2026). We use LMFIT (Newville et al., 2016) to perform spectral fitting. We use Pykonal (White et al., 2020) to calculate the raypath to estimate travel time and cumulative attenuation.

Acknowledgments

We thank Fervo Energy for sharing the data and their approval to publish the research. We thank Avinash Nayak for useful discussions on the magnitude estimates. We thank Folarin Kolawole for the discussions on local structures that helped us interpret the results. We greatly appreciate the constructive suggestions from Gian Maria Bocchini, two anonymous reviewers, and the Editor Brandon Schmandt, which have helped improve the quality of the manuscript. Hilary Chang has been funded by The MathWorks Science Fellowship at the Massachusetts Institute of Technology and the Lamont-Doherty Earth Observatory Postdoctoral Fellowship. This work is supported by the U.S. Department of Energy's Hydrocarbons and Geothermal Energy Office under Contract No. DE-AC02-05CH11231 with Lawrence Berkeley National Laboratory.

References

Abercrombie, R. E. (1995). Earthquake source scaling relationships from 1 to 5 ML using seismograms recorded at 2.5 km depth. *Journal of Geophysical Research*, *100*(B12), 24015–24036. https://doi.org/10.1029/95jb02397

Abercrombie, R. E. (1997). Near-surface attenuation and site effects from comparison of surface and deep borehole recordings. *Bulletin of the Seismological Society of America*, *87*(3), 731–744. https://doi.org/10.1785/bssa0870030731

Abercrombie, R. E. (1998). A summary of attenuation measurements from borehole recordings of earthquakes: The 10 Hz transition problem. *Pure and Applied Geophysics*, *153*(4), 475–487. https://doi.org/10.1007/s000240050204

Abercrombie, R. E. (2014). Stress drops of repeating earthquakes on the San Andreas fault at Parkfield. *Geophysical Research Letters*, *41*(24), 8784–8791. https://doi.org/10.1002/2014gl062079

Abercrombie, R. E. (2015). Investigating uncertainties in empirical Green's function analysis of earthquake source parameters. *Journal of Geophysical Research*, *120*(6), 4263–4277. https://doi.org/10.1002/2015jb011984

Abercrombie, R. E. (2021). Resolution and uncertainties in estimates of earthquake stress drop and energy release. *Philosophical Transactions of the Royal Society of London*, *379*(2196), 20200131. https://doi.org/10.1098/rsta.2020.0131

Abercrombie, R. E., Baltay, A., Chu, S., Taira, T., Bindi, D., Boyd, O. S., et al. (2025). Overview of the SCEC/USGS community stress drop validation study using the 2019 Ridgecrest earthquake sequence. *Bulletin of the Seismological Society of America*, *115*(3), 734–759. https://doi.org/10.1785/0120240158

Abercrombie, R. E., & Baltay, A. S. (2025). Magnitude, depth, and methodological variations of spectral stress drop within the SCEC/USGS community stress drop validation study using the 2019 Ridgecrest earthquake sequence. *Bulletin of the Seismological Society of America*.

Abercrombie, R. E., Bannister, S., Ristau, J., & Doser, D. (2016). Variability of earthquake stress drop in a subduction setting, the Hikurangi margin, New Zealand. *Geophysical Journal International*, *ggw393*.

Abercrombie, R. E., & Leary, P. (1993). Source parameters of small earthquakes recorded at 2.5 km depth, Cajon Pass, southern California: Implications for earthquake scaling. *Geophysical Research Letters*, *20*(14), 1511–1514. https://doi.org/10.1029/93gl00367

Abercrombie, R. E., Trugman, D. T., Shearer, P. M., Chen, X., Zhang, J., Pennington, C. N., et al. (2021). Does earthquake stress drop increase with depth in the crust? *Journal of Geophysical Research: Solid Earth*, *126*(10), e2021JB022314. https://doi.org/10.1029/2021jb022314

Abukrat, Y., Sinitsyn, P., Reshef, M., & Lellouch, A. (2023). Applications and limitations of distributed acoustic sensing in shallow seismic surveys and monitoring. *Geophysics*, *88*(6), WC1–WC12. https://doi.org/10.1190/geo2022-0574.1

Ahn, B. S., Kang, T.-S., & Yoo, H. J. (2025). Source parameter estimation using site-corrected source spectra for the 2019 Ridgecrest earthquake sequence in Southern California. *Bulletin of the Seismological Society of America*, *115*(3), 927–946. https://doi.org/10.1785/0120240157

Aki, K., & Richards, P. G. (2002). *Quantitative seismology*. University Science Books.

Anderson, J. G., & Hough, S. E. (1984). A model for the shape of the Fourier amplitude spectrum of acceleration at high frequencies. *Bulletin of the Seismological Society of America*, *74*(5), 1969–1993. https://doi.org/10.1785/bssa0740051969

Asano, K., & Iwata, T. (2011). Characterization of stress drops on asperities estimated from the heterogeneous kinematic slip model for strong motion prediction for inland crustal earthquakes in Japan. *Pure and Applied Geophysics*, *168*(1), 105–116. https://doi.org/10.1007/s00024-010-0116-y

Baird, A., Stork, A., Horne, S., Naldrett, G., Kendall, J.-M., Wookey, J., et al. (2020). Characteristics of microseismic data recorded by distributed acoustic sensing systems in anisotropic media. *Geophysics*, *85*(4), KS139–KS147. https://doi.org/10.1190/geo2019-0776.1

Bakku, S. K. (2015). *Fracture characterization from seismic measurements in a borehole (unpublished doctoral dissertation)*. Massachusetts Institute of Technology.

Baltay, A., Abercrombie, R., Chu, S., & Taira, T. (2024). The SCEC/USGS community stress drop validation study using the 2019 Ridgecrest earthquake sequence. *Seismica*, *3*(1). https://doi.org/10.26443/seismica.v3i1.1009

Barbour, A. J., McGuire, J. J., Karrenbach, M., McPherson, R. C., Hemphill-Haley, M. A., & Stewart, C. (2025). Earthquake magnitude and source parameter estimation with a distributed acoustic sensing dataset in the Gorda subduction zone. *Bulletin of the Seismological Society of America*.

Bethmann, F., Deichmann, N., & Mai, P. M. (2012). Seismic wave attenuation from borehole and surface records in the top 2.5 km beneath the city of Basel, Switzerland. *Geophysical Journal International*, *190*(2), 1257–1270. https://doi.org/10.1111/j.1365-246x.2012.05555.x

Boatwright, J. (1978). Detailed spectral analysis of two small New York State earthquakes. *Bulletin of the Seismological Society of America*, *68*(4), 1117–1131. https://doi.org/10.1785/BSSA0680041117

Boatwright, J. (1980). A spectral theory for circular seismic sources; simple estimates of source dimension, dynamic stress drop, and radiated seismic energy. *Bulletin of the Seismological Society of America*, *70*(1), 1–27. https://doi.org/10.1785/BSSA0700010001

Brune, J. N. (1970). Tectonic stress and the spectra of seismic shear waves from earthquakes. *Journal of Geophysical Research*, *75*(26), 4997–5009. https://doi.org/10.1029/jb075i026p04997

Byerley, G., Monk, D., Aaron, P., & Yates, M. (2018). Time-lapse seismic monitoring of individual hydraulic frac stages using a downhole DAS array. *The Leading Edge*, *37*(11), 802–810. https://doi.org/10.1190/tle37110802.1

Calderoni, G., & Abercrombie, R. E. (2023). Investigating spectral estimates of stress drop for small to moderate earthquakes with heterogeneous slip distribution: Examples from the 2016–2017 Amatrice earthquake sequence. *Journal of Geophysical Research: Solid Earth*, *128*(6), e2022JB025022. https://doi.org/10.1029/2022jb025022

Candela, T., Renard, F., Bouchon, M., Schmittbuhl, J., & Brodsky, E. E. (2011). Stress drop during earthquakes: Effect of fault roughness scaling. *Bulletin of the Seismological Society of America*, *101*(5), 2369–2387. https://doi.org/10.1785/0120100298

Chang, H., Abercrombie, R. E., & Nakata, N. (2025). Importance of considering near-surface attenuation in earthquake source parameter estimation: Insights from kappa at a dense array in Oklahoma. *Bulletin of the Seismological Society of America*, *115*(3), 947–964. https://doi.org/10.1785/0120240137

21699356, 2026, 9, Downloaded from https://agupubs.onlinelibrary.wiley.com/doi/10.1029/2026JB034276, Wiley Online Library on [23/10/2026]. See the Terms and Conditions (https://onlinelibrary.wiley.com/terms-and-conditions) on Wiley Online Library for rules of use; OA articles are governed by the applicable Creative Commons License

Chang, H., Abercrombie, R. E., Nakata, N., Pennington, C. N., Kemna, K. B., Cochran, E. S., & Harrington, R. M. (2023). Quantifying site effects and their influence on earthquake source parameter estimations using a dense array in Oklahoma. *Journal of Geophysical Research*, *128*(9), e2023JB027144. https://doi.org/10.1029/2023JB027144

Chang, H., & Nakata, N. (2022). Investigation of time-lapse changes with DAS borehole data at the Brady geothermal field using deconvolution interferometry. *Remote Sensing*, *14*(1), 185. https://doi.org/10.3390/rs14010185

Chang, H., & Nakata, N. (2024). Urban site characterization using DAS dark fibers on the MIT campus in Cambridge, Massachusetts. *The Leading Edge*, *43*(11), 747–756. https://doi.org/10.1190/tle43110747.1

Chang, H., Nakata, N., Abercrombie, R., Dadi, S., & Titov, A. (2026). Cape EGS: Seismic attenuation profile and DAS microseismic P-wave spectra [Dataset]. *Geothermal Data Repository, Lamont Doherty Earth Observatory*. Retrieved from https://gdr.openei.org/submissions/1823

Chen, X. (2023). Source parameter analysis using distributed acoustic sensing–an example with the PoroTomo array. *Geophysical Journal International*, *233*(3), 2208–2214. https://doi.org/10.1093/gji/ggad061

Cole, S., Karrenbach, M., Kahn, D., Rich, J., Silver, K., & Langton, D. (2018). Source parameter estimation from DAS microseismic data. In *SEG international Exposition and Annual Meeting* (pp. SEG–2018).

Correa, J., Pevzner, R., Bona, A., Tertyshnikov, K., Freifeld, B., Robertson, M., & Daley, T. (2019). 3D vertical seismic profile acquired with distributed acoustic sensing on tubing installation: A case study from the CO2CRC Otway Project. *Interpretation*, *7*(1), SA11–SA19. https://doi.org/10.1190/int-2018-0086.1

Dadi, S., Norbeck, J., Titov, A., Dyer, B., Mohammadi, A., Geng, Y., et al. (2024). Microseismic monitoring during a next generation enhanced geothermal System at Cape Modern, Utah. *GRC Transactions*, *48*.

Daley, T. M., Miller, D., Dodds, K., Cook, P., & Freifeld, B. (2016). Field testing of modular borehole monitoring with simultaneous distributed acoustic sensing and geophone vertical seismic profiles at Citronelle, Alabama. *Geophysical Prospecting*, *64*(5), 1318–1334. https://doi.org/10.1111/1365-2478.12324

Dean, T., Cuny, T., & Hartog, A. H. (2017). The effect of gauge length on axially incident P-waves measured using fibre optic distributed vibration sensing. *Geophysical Prospecting*, *65*(1), 184–193. https://doi.org/10.1111/1365-2478.12419

Dreger, D., Nadeau, R. M., & Chung, A. (2007). Repeating earthquake finite source models: Strong asperities revealed on the San Andreas Fault. *Geophysical Research Letters*, *34*(23). https://doi.org/10.1029/2007GL031353

Eshelby, J. D. (1957). The determination of the elastic field of an ellipsoidal inclusion, and related problems. *Proceedings of the Royal Society of London — Series A: Mathematical and Physical Sciences*, *241*(1226), 376–396. https://doi.org/10.1098/rspa.1957.0133

Fercho, S., Matson, G., McConville, E., Rhodes, G., Jordan, R., & Norbeck, J. (2024). Geology, temperature, geophysics, stress orientations, and natural fracturing in the Milford Valley, UT informed by the drilling results of the first horizontal wells at the Cape Modern Geothermal Project. In *Proceedings, 49th Stanford Workshop on Geothermal Reservoir Engineering*.

Goertz-Allmann, B. P., & Wiemer, S. (2013). Geomechanical modeling of induced seismicity source parameters and implications for seismic hazard assessment. *Geophysics*, *78*(1), KS25–KS39. https://doi.org/10.1190/geo2012-0102.1

Gök, R., Walter, W. R., Barno, J., Downie, C., Mellors, R. J., Mayeda, K., et al. (2024). Reliable earthquake source parameters using distributed acoustic sensing data derived from coda envelopes. *Seismological Research Letters*, *95*(4), 2208–2220. https://doi.org/10.1785/0220230270

Hanks, T. C., & Kanamori, H. (1979). A moment magnitude scale. *Journal of Geophysical Research*, *84*(B5), 2348–2350. https://doi.org/10.1029/jb084ib05p02348

Hartog, A. (2017). *An introduction to distributed optical fibre sensors*. CRC Press.

Hartzell, S. H. (1978). Earthquake aftershocks as Green's functions. *Geophysical Research Letters*, *5*(1), 1–4. https://doi.org/10.1029/gl005i001p00001

Hough, S. (1997). Empirical Green's function analysis: Taking the next step. *Journal of Geophysical Research*, *102*(B3), 5369–5384. https://doi.org/10.1029/96jb03488

Hough, S., & Anderson, J. (1988). High-frequency spectra observed at Anza, California: Implications for Q structure. *Bulletin of the Seismological Society of America*, *78*(2), 692–707. https://doi.org/10.1785/bssa0780020692

Ide, S., Beroza, G. C., Prejean, S. G., & Ellsworth, W. L. (2003). Apparent break in earthquake scaling due to path and site effects on deep borehole recordings. *Journal of Geophysical Research*, *108*(B5). https://doi.org/10.1029/2001jb001617

Jin, G., & Roy, B. (2017). Hydraulic-fracture geometry characterization using low-frequency DAS signal. *The Leading Edge*, *36*(12), 975–980. https://doi.org/10.1190/tle36120975.1

Jongmans, D., & Malin, P. E. (1995). Microearthquake S-wave observations from 0 to 1 km in the Varian well at Parkfield, California. *Bulletin of the Seismological Society of America*, *85*(6), 1805–1820. https://doi.org/10.1785/bssa0850061805

Kaneko, Y., & Shearer, P. (2014). Seismic source spectra and estimated stress drop derived from cohesive-zone models of circular subshear rupture. *Geophysical Journal International*, *197*(2), 1002–1015. https://doi.org/10.1093/gji/ggu030

Kaneko, Y., & Shearer, P. (2015). Variability of seismic source spectra, estimated stress drop, and radiated energy, derived from cohesive-zone models of symmetrical and asymmetrical circular and elliptical ruptures. *Journal of Geophysical Research: Solid Earth*, *120*(2), 1053–1079. https://doi.org/10.1002/2014jb011642

Karrenbach, M., Cole, S., Ridge, A., Boone, K., Kahn, D., Rich, J., et al. (2019). Fiber-optic distributed acoustic sensing of microseismicity, strain and temperature during hydraulic fracturing. *Geophysics*, *84*(1), D11–D23. https://doi.org/10.1190/geo2017-0396.1

Ko, Y.-T., Kuo, B.-Y., & Hung, S.-H. (2012). Robust determination of earthquake source parameters and mantle attenuation. *Journal of Geophysical Research*, *117*(B4), B04304. https://doi.org/10.1029/2011jb008759

Kwiatek, G., Bulut, F., Bohnhoff, M., & Dresen, G. (2014). High-resolution analysis of seismicity induced at Berlín geothermal field, El Salvador. *Geothermics*, *52*, 98–111. https://doi.org/10.1016/j.geothermics.2013.09.008

Lee, J., Tsai, V. C., Trugman, D. T., Hirth, G., & Chatterjee, A. (2025). Fault network geometry modulates earthquake source spectra across scales. *Geophysical Research Letters*, *52*(12), e2025GL115592. https://doi.org/10.1029/2025gl115592

Lellouch, A., Schultz, R., Lindsey, N. J., Biondi, B., & Ellsworth, W. L. (2021). Low-magnitude seismicity with a downhole distributed acoustic sensing array—Examples from the FORGE geothermal experiment. *Journal of Geophysical Research: Solid Earth*, *126*(1), e2020JB020462. https://doi.org/10.1029/2020jb020462

Lellouch, A., Yuan, S., Ellsworth, W. L., & Biondi, B. (2019). Velocity-based earthquake detection using downhole distributed acoustic sensing—Examples from the San Andreas Fault Observatory at depth. *Bulletin of the Seismological Society of America*, *109*(6), 2491–2500. https://doi.org/10.1785/0120190176

Li, J., Zhu, W., Biondi, E., & Zhan, Z. (2023). Earthquake focal mechanisms with distributed acoustic sensing. *Nature Communications*, *14*(1), 4181. https://doi.org/10.1038/s41467-023-39639-3

Li, M., Wang, H., & Tao, G. (2015). Current and future applications of distributed acoustic sensing as a new reservoir geophysics tool. *The Open Petroleum Engineering Journal*, *8*(1), 272–281. https://doi.org/10.2174/1874834120150625e008

21699356, 2026, 9, Downloaded from https://agupubs.onlinelibrary.wiley.com/doi/10.1029/2026JB034276, Wiley Online Library on [23/10/2026]. See the Terms and Conditions (https://onlinelibrary.wiley.com/terms-and-conditions) on Wiley Online Library for rules of use; OA articles are governed by the applicable Creative Commons License

Lindsey, N. J., Rademacher, H., & Ajo-Franklin, J. B. (2020). On the broadband instrument response of fiber-optic DAS arrays. *Journal of Geophysical Research: Solid Earth*, *125*(2), e2019JB018145. https://doi.org/10.1029/2019jb018145

Lior, I. (2024). Accurate magnitude and stress drop using the spectral ratios method applied to distributed acoustic sensing. *Geophysical Research Letters*, *51*(1), e2023GL105153. https://doi.org/10.1029/2023gl105153

Lior, I., Rivet, D., Ampuero, J.-P., Sladen, A., Barrientos, S., Sánchez-Olavarría, R., et al. (2023). Magnitude estimation and ground motion prediction to harness fiber optic distributed acoustic sensing for earthquake early warning. *Scientific Reports*, *13*(1), 424. https://doi.org/10.1038/s41598-023-27444-3

Lior, I., & Ziv, A. (2018). The relation between ground motion, earthquake source parameters, and attenuation: Implications for source parameter inversion and ground motion prediction equations. *Journal of Geophysical Research: Solid Earth*, *123*(7), 5886–5901. https://doi.org/10.1029/2018jb015504

Luo, B., Jin, G., & Stanek, F. (2021). Near-field strain in distributed acoustic sensing-based microseismic observation. *Geophysics*, *86*(5), P49–P60. https://doi.org/10.1190/geo2021-0031.1

Madariaga, R. (1976). Dynamics of an expanding circular fault. *Bulletin of the Seismological Society of America*, *66*(3), 639–666. https://doi.org/10.1785/bssa0660030639

Madariaga, R. (1979). On the relation between seismic moment and stress drop in the presence of stress and strength heterogeneity. *Journal of Geophysical Research*, *84*(B5), 2243–2250. https://doi.org/10.1029/jb084ib05p02243

Martuganova, E., Norden, B., Blöcher, G., & Krawczyk, C. M. (2024). Enhanced geothermal reservoir characterization using wireline distributed acoustic sensing. *Distributed Acoustic Sensing in Borehole Geophysics*, 385–398.

Mateeva, A., Lopez, J., Potters, H., Mestayer, J., Cox, B., Kiyashchenko, D., et al. (2014). Distributed acoustic sensing for reservoir monitoring with vertical seismic profiling. *Geophysical Prospecting*, *62*(4-Vertical Seismic Profiling and Microseismicity Frontiers), 679–692. https://doi.org/10.1111/1365-2478.12116

Miller, J. (2018). Utah FORGE: 2D and 3D seismic data. Geothermal data repository. *Energy and Geoscience Institute at the University of Utah*. https://doi.org/10.15121/1452746

Moein, M. J., Langenbruch, C., Schultz, R., Grigoli, F., Ellsworth, W. L., Wang, R., et al. (2023). The physical mechanisms of induced earthquakes. *Nature Reviews Earth and Environment*, *4*(12), 847–863. https://doi.org/10.1038/s43017-023-00497-8

Mohammadi, A., Chen, X., Nakata, N., Dadi, S., & Energy, F. (2025). Focal mechanism and stress analysis of the Cape site, Utah. In *Proceedings, 50th Stanford Workshop on Geothermal Reservoir Engineering*.

Mosconi, F., Tinti, E., Supino, M., Gabriel, A.-A., Casarotti, E., Meier, M.-A., et al. (2026). Discriminating dynamic rupture arrest in fluid-induced microearthquakes using spectral inversion. *Earth and Planetary Science Letters*, *678*, 119816. https://doi.org/10.1016/j.epsl.2025.119816

Moyer, P. A., Boettcher, M. S., McGuire, J. J., & Collins, J. A. (2018). Spatial and temporal variations in earthquake stress drop on Gofar Transform Fault, East Pacific Rise: Implications for fault strength. *Journal of Geophysical Research: Solid Earth*, *123*(9), 7722–7740. https://doi.org/10.1029/2018jb015942

Nakata, N., Chang, H., Wu, S.-M., Bi, Z., Chen, L.-W., Soom, F., et al. (2025). Fracture characterization revealed by microseismicity at Cape Modern geothermal field, Utah. In *Proceedings, 50th Stanford Workshop on Geothermal Reservoir Engineering*.

Nakata, N., Wu, S.-M., Hopp, C., Robertson, M., & Dadi, S. (2024). Microseismicity observation and characterization at Cape Modern and Utah FORGE. In *Proceedings, 49th Stanford Workshop on Geothermal Reservoir Engineering*.

Nayak, A., Correa, J., & Ajo-Franklin, J. (2024). Seismic magnitude estimation using low-frequency strain amplitudes recorded by DAS arrays at far-field distances. *Bulletin of the Seismological Society of America*, *114*(4), 1818–1838. https://doi.org/10.1785/0120230318

Nayak, A., Nakata, N., & Hopp, C. (2026). Monitoring seismic moment release and focal mechanisms at Cape and FORGE EGS sites, Utah. *Bulletin of the Seismological Society of America*. (Accepted for publication).

Newville, M., Stensitzki, T., Allen, D. B., Rawlik, M., Ingargiola, A., & Nelson, A. (2016). LMFIT: Non-linear least-square minimization and curve-fitting for Python [Software]. Retrieved from https://lmfit.github.io/lmfit-py

Park, S.-E., Jung, Y.-H., Nakata, N., Oh, J.-W., & Dyer, B. (2025). Enhancing P-wave velocity model at the Utah Forge EGS site using traveltime tomography and full-waveform inversion of 2D DAS-VSP and 3D surface seismic data. *The Leading Edge*, *44*(4), 256–264. https://doi.org/10.1190/tle44040256.1

Park, S.-E., Nakata, N., Oh, J.-W., & Dyer, B. (2025). P-wave velocity model at Utah FORGE geothermal field using travel-time tomography of DAS-VSP data. *IEEE Transactions on Geoscience and Remote Sensing*.

Pennington, C. N., Chang, H., Rubinstein, J. L., Abercrombie, R. E., Nakata, N., Uchide, T., & Cochran, E. S. (2022). Quantifying the sensitivity of microearthquake slip inversions to station distribution using a dense nodal array. *Bulletin of the Seismological Society of America*, *112*(3), 1252–1270. https://doi.org/10.1785/0120210279

Prieto, G. A. (2022). The multitaper spectrum analysis package in Python. *Seismological Society of America*, *93*(3), 1922–1929. https://doi.org/10.1785/0220210332

Rodríguez Tribaldos, V., Hopp, C., Rinaldi, A. P., Tuinstra, K. B., Lanza, F., Ajo-Franklin, J., et al. (2024). Use of distributed acoustic sensing and distributed strain sensing technologies for geomechanical characterization of rock mass response in mesoscale experiments in underground laboratories: Lessons learned. *Distributed Acoustic Sensing in Borehole Geophysics*, 549–578.

Ruhl, C. J., Abercrombie, R. E., & Shearer, P. M. (2023). Spatially consistent small-scale stress heterogeneity revealed by the 2008 Mogul, Nevada, earthquakes. *The Seismic Record*, *3*(3), 239–248. https://doi.org/10.1785/0320230026

Shapiro, S. A., & Dinske, C. (2021). Stress drop, seismogenic index and fault cohesion of fluid-induced earthquakes. *Rock Mechanics and Rock Engineering*, *54*(10), 5483–5492. https://doi.org/10.1007/s00603-021-02420-3

Shearer, P. M., Abercrombie, R. E., Trugman, D. T., & Wang, W. (2019). Comparing EGF methods for estimating corner frequency and stress drop from P wave spectra. *Journal of Geophysical Research: Solid Earth*, *124*(4), 3966–3986. https://doi.org/10.1029/2018jb016957

Shearer, P. M., Prieto, G. A., & Hauksson, E. (2006). Comprehensive analysis of earthquake source spectra in southern California. *Journal of Geophysical Research*, *111*(B6). https://doi.org/10.1029/2005jb003979

Shearer, P. M., Vandevert, I., Fan, W., Abercrombie, R. E., Bindi, D., Calderoni, G., et al. (2025). Earthquake source spectra estimates vary widely for two Ridgecrest aftershocks because of differences in attenuation corrections. *Bulletin of the Seismological Society of America*, *115*(3), 777–791. https://doi.org/10.1785/0120240134

Strumia, C., Trabattoni, A., Supino, M., Baillet, M., Rivet, D., & Festa, G. (2024). Sensing optical fibers for earthquake source characterization using raw DAS records. *Journal of Geophysical Research: Solid Earth*, *129*(1), e2023JB027860. https://doi.org/10.1029/2023jb027860

van den Ende, M., Trabattoni, A., Baillet, M., & Rivet, D. (2025). An analysis of the dynamic range of distributed Acoustic Sensing for earthquake early warning. *Seismica*, *4*(1). https://doi.org/10.26443/seismica.v4i1.1371

21699356, 2026, 9, Downloaded from https://agupubs.onlinelibrary.wiley.com/doi/10.1029/2026JB034276, Wiley Online Library on [23/10/2026]. See the Terms and Conditions (https://onlinelibrary.wiley.com/terms-and-conditions) on Wiley Online Library for rules of use; OA articles are governed by the applicable Creative Commons License

Vandevert, I. C., Shearer, P. M., & Fan, W. (2025). Ridgecrest aftershock stress drops from P-and S-wave spectral decomposition. *Bulletin of the Seismological Society of America*, *115*(3), 792–804. https://doi.org/10.1785/0120240133

Viegas, G., Abercrombie, R. E., & Kim, W.-Y. (2010). The 2002 M5 Au Sable Forks, NY, earthquake sequence: Source scaling relationships and energy budget. *Journal of Geophysical Research*, *115*(B7). https://doi.org/10.1029/2009jb006799

Wang, H. F., Zeng, X., Miller, D. E., Fratta, D., Feigl, K. L., Thurber, C. H., & Mellors, R. J. (2018). Ground motion response to an M_L 4.3 earthquake using co-located distributed acoustic sensing and seismometer arrays. *Geophysical Journal International*, *213*(3), 2020–2036. https://doi.org/10.1093/gji/ggy102

Wang, L., Kwiatek, G., Renard, F., Guérin-Marthe, S., Rybacki, E., Bohnhoff, M., et al. (2024). Fault roughness controls injection-induced seismicity. *Proceedings of the National Academy of Sciences*, *121*(3), e2310039121. https://doi.org/10.1073/pnas.2310039121

Wang, Y., & Day, S. M. (2017). Seismic source spectral properties of crack-like and pulse-like modes of dynamic rupture. *Journal of Geophysical Research: Solid Earth*, *122*(8), 6657–6684. https://doi.org/10.1002/2017jb014454

White, M. C., Fang, H., Nakata, N., & Ben-Zion, Y. (2020). PyKonal: A Python package for solving the eikonal equation in spherical and Cartesian coordinates using the fast marching method [Software]. *Seismological Research Letters*, *91*(4), 2378–2389. https://doi.org/10.1785/0220190318

Yu, H., Harrington, R. M., Kao, H., Liu, Y., Abercrombie, R. E., & Wang, B. (2020). Well proximity governing stress drop variation and seismic attenuation associated with hydraulic fracturing induced earthquakes. *Journal of Geophysical Research: Solid Earth*, *125*(9), e2020JB020103. https://doi.org/10.1029/2020jb020103

Zhai, Q., Yin, J., Yang, Y., Atterholt, J. W., Li, J., Husker, A., & Zhan, Z. (2025). Comprehensive evaluation of DAS amplitude and its implications for earthquake early warning and seismic interferometry. *Journal of Geophysical Research: Solid Earth*, *130*(4), e2024JB030288. https://doi.org/10.1029/2024jb030288

Zhan, Z. (2020). Distributed acoustic sensing turns fiber-optic cables into sensitive seismic antennas. *Seismological Research Letters*, *91*(1), 1–15. https://doi.org/10.1785/0220190112

Zhang, Z., White, M. C., Bai, T., Qiu, H., & Nakata, N. (2023). Characterizing microearthquakes induced by hydraulic fracturing with hybrid borehole DAS and three-component geophone data. *IEEE Transactions on Geoscience and Remote Sensing*, *61*, 1–15. https://doi.org/10.1109/tgrs.2023.3264931

Zhu, W., Biondi, E., Li, J., Yin, J., Ross, Z. E., & Zhan, Z. (2023). Seismic arrival-time picking on distributed acoustic sensing data using semi-supervised learning. *Nature Communications*, *14*(1), 8192. https://doi.org/10.1038/s41467-023-43355-3

Zielke, O., Galis, M., & Mai, P. M. (2017). Fault roughness and strength heterogeneity control earthquake size and stress drop. *Geophysical Research Letters*, *44*(2), 777–783. https://doi.org/10.1002/2016gl071700

21699356, 2026, 9, Downloaded from https://agupubs.onlinelibrary.wiley.com/doi/10.1029/2026JB034276, Wiley Online Library on [23/10/2026]. See the Terms and Conditions (https://onlinelibrary.wiley.com/terms-and-conditions) on Wiley Online Library for rules of use; OA articles are governed by the applicable Creative Commons License